1-1-2009

# Heterogeneous Drive Mechanisms for Novel Locomotion in Rough Terrain

Roy Godzdanker
*University of Denver*

# Heterogeneous Drive Mechanisms for Novel Locomotion in Rough Terrain

_____

A Thesis

Presented to

The Faculty of Engineering and Computer Science

University of Denver

_____

In Partial Fulfillment

of the Requirements for the degree

Masters of Science

_____

by

Roy Godzdanker

August, 2009

Advisor: Richard Voyles, Ph.D.

Author: Roy Godzdanker
Title: Heterogeneous Drive Mechanisms for Novel Locomotion in Rough Terrain
Advisor: Richard Voyles, Ph.D.
Degree Date: August, 2009

## ABSTRACT

The smaller the robot the easier it is for it to access voids in a collapsed structure, however small size brings a host of other problems related to constrained resources. One of the primary constraints on small robots is limited motive power to surmount obstacles and navigate rough terrain. This thesis examines the addition of bulk motive force actuators to existing locomotion platforms and the impact of these heterogeneous actuators on conventional steering methods. The steering methods examined are those associated with skid steered vehicles and differential drive vehicles. In developing the Crabinator, a robot composed of a limbed crawler module and a single track drive module, it appeared that the resulting robot did not fit in the regime of differential drive. For that reason the heterogeneous differential drive class was developed. Similarly for the water hammer active tether module this system also did not appear to be a heterogeneous differential drive or skid steered vehicles. This system turned out to be even more general hence the more general class of heterogeneous drive vehicles which has input of accelerations rather then velocities as the previously mentioned classes.

Acknowledgements:

I have benefited from the advice, friendship, and support of quite a number of people throughout my years at the University of Denver and will surely continue keeping in touch with those people wherever my life will take me. First foremost I would like to thank my Advisor Dr. Richard Voyles for taking me on as his first graduate student at the University of Denver and continually challenging and pushing my "comfort zone." Additionally I would like to thank my fellow graduate students that have helped me through some tough patches. In particular would like to thank Jaewook Bae, Ian Welch, and Matt Openorth for there technical help and the occasional beer we had to unwind.

Finally and most importantly I would like to thank my family that have helped me stay on tracked and motivated throughout this roller coaster ride

# Table of Contents

# List of Tables

# List of Figures

# Chapter 1
# Introduction

The field of robotics is a rapidly growing, multi-faceted field. From Ancient Greece to the present day, robots have been and still are described and designed as machines to help humankind. When it comes to helping humankind, the capabilities of robots have evolved over time. Beginning in the late sixties, UNIMATE has developed robots to assemble cars in factories. Today, robots are used in a wide range of tasks, including: performing surgeries, aerial and ground exploration, household cleaning, and even building objects in outer space. Each one of these fields presents its own set of challenges. This thesis focuses on only one area of robotics, ground exploration.

## 1.1 Motivation and Rationale

The use of robots in ground exploration presents many challenges, particularly the exploration of rough and unknown terrains. In robotics, "unknown terrain" is defined as any terrain where the robot or the human operator has no prior knowledge of the layout or where obstacles might lay. "Rough terrain" is more ambiguous to define as it is correlated to the shape size and capabilities of the robot. Robots are used in ground

exploration because they can replace humans for exploration of environments that could put humans at risk of injury or death.

Some examples where robots have been used for exploration and require further research include the following: planetary exploration, war zones, collapsed buildings, and collapsed mines. Planetary exploration is one application where robots have been used because they are relatively cheaper to send into space and absolutely safer than sending humans to other planets. However, the problem with planetary robots is that they are very slow. On a good day, Spirit and Opportunity traversed only 70 feet [1]. The primary reasons for limited speed are the difficulty of navigating in a rough terrain, limited communication with the operators on Earth, and limited on board computational capabilities. Another example where ground robots are used is in military operations. The US Army, with on-going wars in Iraq and Afghanistan, has invested a great deal of money in autonomous ground robots to replace soldiers in dangerous environments. The military is pursuing the use of robots in close quarter urban combat environments and convoy transportation. Some military robots are meant to replace existing vehicles in the field and this work is motivated with the DARPA grand challenge competition [2]. Other robots, such as the Packbot, [3] are intended to identify Improvised Explosive Devices (IED).

Robots have also been used for exploration of collapsed buildings, such as those encountered following major earthquakes. These energetically disassembled environments create very difficult rough terrain for search and rescue operations. The potential for secondary collapses from the instabilities present in collapsed buildings, mixed debris fields, and small passageways that may open to larger life sustaining voids

all contribute to difficult terrain for both humans and robots to navigate. A secondary collapse could occur when the roof of a building falls down onto another floor of a building and ends up being supported by a single wall or column from the floor beneath as seen in Figure 1.

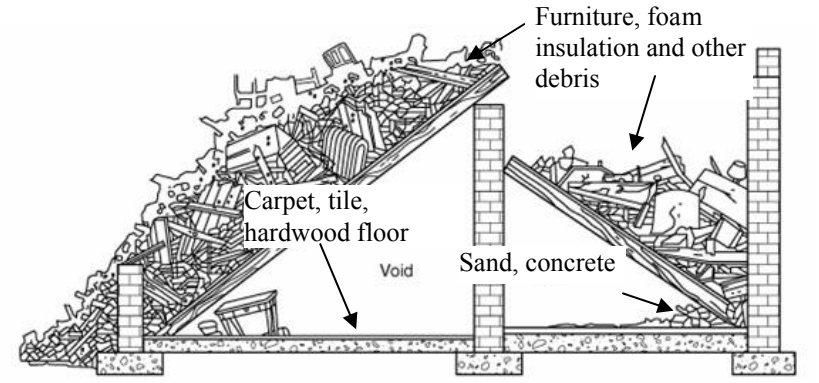


**Figure 1:** Secondary Collapse Scenario with a mixed debris in the

In this scenario, sending in a human or canine is very dangerous to both the rescuer(s) and any possible survivors that could be in the void. A mixed debris field is another challenge of collapsed buildings where search and rescue operators must contend with sand, dust, carpet, furniture and many other building materials. Hence, a robot for this environment must be adaptable for traversing different types of terrains. Another challenge of collapsed terrains is that small voids could lead to larger voids that may sustain life, as seen in Figure 2 below. This scenario requires a robot that is small enough to fit into narrow passages.

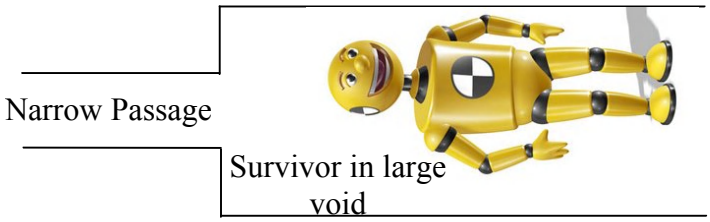


**Figure 2:** Small void opening up to large void

Urban Search and Rescue ("USAR") is the branch of robotics research that focuses on developing robots to supplement and eventually replace humans and dogs in the search for survivors in dangerous environments. The work presented in this thesis is focused on USAR robotics. The motivation behind this research focus is two-fold. First, development of robots for USAR is very complex and a research rich field. Second, the development of robots for USAR environments has a direct impact on humanity. Better robots will help protect search and rescue workers and increase the odds of finding more survivors in disaster situations.

### 1.2 Problem Statement

As can been seen from the previous section there are many obstacles to overcome in designing a robot for USAR environments. These obstacles include locomotion, size and weight. Smaller robots can more easily access voids in a collapsed structure, however, small size brings a host of other issues related to limited resources. One of the primary constraints of small robots is limited motive power to surmount obstacles and navigate rough terrain. This thesis presents work developing drive methods to augment small, resource constrained robots. Figure 3 illustrates the motivation for developing new drive methods that enable smaller robots to access areas that are currently not accessible due to limited mobility.

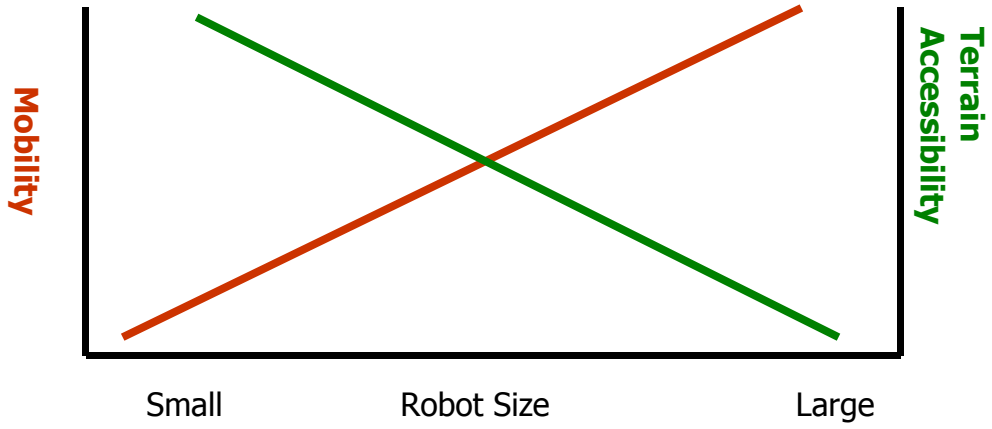


**Figure 3:** Comparison between robot size and terrain accessibility

### 1.3 Proposed Solution

To solve the limited mobility problem of resource constrained robots, this thesis presents work on (1) the development of bulk motive force actuator and (2) a method by which to control different classes of bulk motive force actuators. Bulk motive force actuators are those that only possess one Degree of Freedom ("DOF"), perfect for enhancing lift/torque capability of a robot to surmount large obstacles, but incapable of steering due to the modules single DOF configuration. The host robot equipped with more sophisticated actuators must take over the steering capabilities of the system as a whole.

In developing new bulk motive actuators it was initially thought that the control of the resulting system could be modeled based on existing theory of differential and skid steered drive vehicles. However, the resulting systems actually violated many of the assumptions that define skid steered and differential drive mechanisms and hence leading to the development of two new steering models: heterogeneous differential drive and heterogonous drive.

## 1.4 Contributions

This thesis offers three contributions to the field of robotics as a whole, but more specifically to the field of urban search and rescue. These contributions are:

1) Extension of previous work on differential drive, to include heterogeneous and differential heterogeneous drive regimes as presented in Chapter five.
2) Improving and enhancing the capabilities of the TerminatorBot with bulk motive actuators, which extend capabilities in urban search and rescue by implementing side slipping locomotion. An example of one of this bulk motive module is the Crabinator and is explained in greater detail in Chapter four.
3) Development of a framework for Heterogeneous Drive steering control for non-differential mechanisms, based on mass matrix control.

## 1.5 Thesis Outline

The remainder of this thesis is organized in the following manner. Chapter two reviews existing search and rescue robots and their locomotion regimes. Chapter three explains the equations used to govern differential drive and skid steered vehicles. Chapter four presents work on the development of the bulk motive module or Crabinator drive modules for resource constrained robots, motivated by the Utah mine collapse. Chapter five introduces a heterogeneous differential drive model for controlling augmented resource constrained robots such as the one presented in chapter four. Chapter six expands upon the idea of heterogeneous drive presented in chapter five and explains the formulation of the augmented object and how it is used to develop the mass matrix. This

mass matrix would be essential for implementing real-time control of a resource constrained robot augmented with an impulse drive module. Additionally, chapter six also presents the results achieved with planer one-arm and two-arm models of a heterogeneous drive robot controlled by impulsive forces. Finally, chapter seven summarizes my findings and sets forth recommendations for future work in this area.

## Chapter 2
## Previous Work: Existing Robots

One of the design criteria for developing USAR robots is the actuation necessary for forward locomotion. The overall size, weight and mobility of the robot must be considered when choosing the appropriate actuation method. Some actuation methods are more mechanically complex and will, therefore, lead to a larger and heavier robot. Small, light robots are needed for exploring small areas and avoiding secondary collapses. Versatile actuators are needed for traversing the varied terrain found in USAR environments. This chapter presents some of the existing robots used in USAR, along with their pros and cons as related to their size and complexity and mobility.

One way to classify robots is based on their portability [4,5]. This classification system labels robots as either "man–packable", "man-portable", or "not man portable". By classifying robots based on portability, they are also indirectly being classified by size and weight, which is important. In addition to small size, this thesis also investigates the effectiveness of different actuation methods. For this reason, the robots introduced here are organized by actuation methods. Five classes of robots will be presented and some examples of existing robots of these classes will be presented. These classes are (1)

wheeled, (2) tracked, (3) limbed, (4) hybrids of wheeled, tracked, and limbed, and (5) snake robots.

### 2.1 Wheeled Robots

Wheeled robot platforms are among the simplest to construct and were among the first robots developed. In addition to being relatively simple, mechanically, they also tend to be easy to control. There are three common models for controlling wheeled vehicles, skid-steered, differential drive, and the Ackerman method. ATRV Jr., as seen in Figure 4, which is used extensively in academia as a testing platform, is an example of a skid-steered vehicle. SCOUT [6], also pictured in Figure 4, is an example of a differential drive robot.

**Figure 4:** Example of wheeled robots ATRV Jr. on left and SCOUT on right [44 45]

Ackerman steering [39], the method used in cars, controls the vehicle by turning the front two wheels. All of the robots in the DARPA grand challenge based on commercial automobiles had Ackerman steering systems.

The advantages of wheeled robots are their ease of control, and they are mechanically simple to build. Additionally, wheeled robots can be designed in any shape or size, as exhibited by the ATRV JR., SCOUT and many RC cars found at hobby shops.

Yet, one of the main draw-backs of wheeled robots is that they require continuously traversable terrain. A continuous traversable path for a wheeled robot is one that does not constrain obstacles greater than one half the wheel diameter of the robot. Big robots, such as the ATRV Jr., have big wheels and hence can surmount large obstacles while smaller robots, such as the SCOUT, will get stuck if they encounter obstacles larger than one inch in height. Wheeled robots are also prone to high centering. This occurs when the robot traverses over an obstacle that then gets stuck on the bottom of the robot leading to loss of ground contact between the drive wheels and the ground. Then the wheels spin in place and the vehicle is unable to continue its mission. For this reason, wheeled robots are generally larger than other robot classes in order for them to be able to surmount any reasonable sized obstacles and avoid high centering.

### 2.2 Tracked Robots

Tracked robots are much more common in the arena of search and rescue because their design is only slightly more complex than wheeled robots, yet remain simple to control. Tracked vehicles are typically designed with skid-steered actuation. Tracked vehicles are similar to wheeled vehicle designs. except that a toothed belt wraps around the two wheels on the same side, forming a continuous path for traction. The addition of tracks eliminates some, but not all, high centering situations that would cause a wheeled vehicle to fail in the field. With wheeled locomotion, the contact points are idealized as four contact points (assuming no slip) while with tracked vehicles they are two parallel plains. With the contact point on each side of the robot considered as a plain, high centering along the parallel plains will only occur if an obstacle is located entirely between the two plains. To help eliminate the possibility of high centering on the center

plain where no actuation is occurring robots are being developed with wider tracks to help minimize the non active surfaces of the robot which cause high centering.

The Foster-Miller SOLEM, seen in Figure 5, [7] is an example of a commercially produced, tracked vehicle. An important aspect of the SOLEM is the front circular contour, common in many other tracked vehicles. The circular front profile still limits the tracked robot, as also occurs with wheeled robots, in that it cannot surmount any obstacle greater then one half the diameter of the front wheel.

**Figure 5:** Tracked robot SOLEM [46]

Innovative methods have been developed to mitigate the obstacle height limit. For example, the Inuktun MicroVGTV [4,5], seen in Figure 6, is a shape-shifting, tracked robot. The shape sifting design of the Micro VGTV allows its front to rise higher than the rear, helping increase the number of obstacles it can surmount. In the typical flat configuration, the MICRO VGTV can only surmount obstacles that are approximately two inches tall. Alternatively, the shape-shifting design shown in Figure 6 can surmount obstacles as large as five inches under the control of a skilled operator.

**Figure 6:** Inuktun Micro VGTV, a shape shifting tracked robot [47]

### 2.3 Limbed Robots

Limbed robots are bio-inspired devices, sharing human-like traits. The limbs make this class of robots the most versatile of all five categories. Humans are capable of walking over a large range of terrain and over obstacles of different size. A great deal of research has been devoted to the development of two-legged walking robots from Raibert's hopping robot [10] to Honda's walking humanoid ASIMO [11]. Yet with all of the advancements in the field of limbed robots, few have been utilized in USAR environments. Walking, limbed robots are limited in USAR because they require substantial computing power to ensure they do not fall over and can effectively choose where to place their limbs. Additionally, limbed locomotors, like humans, require significant energy just to stand because the robot must continually use its actuators to maintain balance even when not moving.

The TerminatorBot [19], seen in Figure 7, is an example of a robot that uses less power consumption that most other limbed designs.

**Figure 7:** TerminatorBot

The TerminatorBot mimics many cold blooded animals by lying on the ground and using its limbs to crawl. This configuration minimizes energy usage because the robot uses the ground to support the bulk of its weight. The TerminatorBot – or Cylindrical Robot for Autonomous Walking and Lifting during Emergency Response ("CRAWLER") – employs a reconfigurable design philosophy to keep the robot small and light. Small size provides accessibility to spaces otherwise unreachable by humans, canines, or currently available commercial robots. Along with its small size the TerminatorBot employs a reconfigurable design, where the limbs can be used for both locomotion and manipulation. The TerminatorBot consists of two limbs that each have three degrees of freedom. These six degrees of freedom allow for arbitrary manipulation of objects during manipulation and a high degree of configurability of the gait motions during locomotion. In its stowed configuration, the TerminatorBot is cylindrical in shape with a diameter of 75 mm and has an overall length of 205 mm in its tethered configuration. The TerminatorBot is a very small, resource constrained robot and it for this type of robot that the research in the thesis is aimed towards.

BigDog, [12] a robot from Boston Dynamics, is designed to act like a mule, carrying payloads for army soldiers over rough terrain and is yet another example of a bio-inspired limbed robot. BigDog is a four-legged robot capable of carrying over 200 lb loads over very rough terrain. Boston Dynamics is currently developing a smaller version, called LittleDog [13], aimed at the USAR environment and for laboratory testing for devising gaits. BigDog and LittleDog can be seen in Figure 8.

**Figure 8:** BigDog and LittleDog [12,13]

## 2.4 Hybrid Robots

Limbed locomotion is extremely adaptable to uneven terrain, but requires sophisticated control and requires substantial energy even when not moving. Tracked locomotion is highly energy efficient and has proven quite robust in many terrain types encountered in natural and man-made settings, but it is not adaptable in its own right. In fact, there are many environments, particularly where many obstacles are located near each other or are of greater height than that of the tread, that treads alone cannot overcome. The most successful designs for irregular terrains, such as those encountered in collapsed structures and subterranean exploration, have been hybrid designs that incorporate both limbs and tracks. Hybrid design examples include the Omni-Tread [8,9], Helios [15], Redback (Tarantula R/C toy) [16], and the commercially-available PackBot from iRobot [17], all seen in Figure 9.

**Figure 9:** Examples of track-limb hybrids, PackBot, Helios, and Redback [48 49 50]

These hybrids have a common theme. Each employs a relatively sophisticated track mechanism in conjunction with simple limb-like capabilities. Covering an entire robot in tread adds significant mass and complexity. Helios, Redback, and PackBot tread-covered "flippers" gain articulation in one degree of freedom with respect to a central body. The flippers can be used to hoist the body over obstacles or to change the geometry of the device. The Helios includes a third "leg" with more degrees of freedom to maintain balance and navigate large obstacles. The addition of these limb-like behaviors greatly enhances mobility in irregular terrain for all of these hybrid robots.

Another bio-inspired, hybrid search and rescue robot is the Rhex [41]. This cockroach inspired robot has six curved legs actuated by a single motor. This configuration causes the legs to act like a single spoke wheel. Rhex maneuvers around the environment as a cockroach does by alternating which three legs are in contact with

the ground therefore always maintaining a tripod of support. This helps make Rhex one of the faster search and rescue robots currently on the market in terms of locomotion speed. A remaining flaw of Rhex is its high centering due to a large dead space of non-actuating surfaces.

### 2.5 Snake Robots

Snake robots are generally multi-segmented and mimic the locomotion of snakes. The Omni-Tread [8], seen in Figure 10, and the Soryu [42] are examples of snake robots.

**Figure 10:** Omni-Tread 4 a tracked snake robot

Both the Omni-Tread [8] and Souryu [42] consist of drive modules that are almost completely covered by treads. The Omni-Tread has a square cross section and is covered on all four sides with multiple, synchronized treads that are commonly driven so they move in unison, regardless of which side, or sides, are in contact with the ground. The Souryu, on the other hand, has a higher aspect ratio, rectangular cross section and is covered on two sides, by one wide, continuous tread. Both robots attempt to minimize "dead" areas that do not actively drive the robot forward. Both the Omni-Tread and the Souryu are similar to snakes in that they consist of multiple tread modules connected by articulated linkages. The linkages between the tread modules act like simple limbs, allowing the treads to "step" over obstacles and chasms as well as providing steering.

One advantage of snake robots is that, similar to biological snakes and reptiles, they use the ground to support their weight. This allows for more efficient energy use than is possible with traditional limbed systems. Hirose [11] has designed many snake robots based on the concept of multi-segmented module and has developed novel actuators for the intra-segment of the robots. A new robot was recently developed based on the concept of toroidal skin [18]. In this case, the skin wraps around the robot and travels through the inside of the body which is similar to how an ameba moves in nature. One disadvantage of all segmented snake robots is that control generally requires many operators and implementation of autonomous locomotion is also very difficult.

# Chapter 3
# Differential and Skid Steered Drive Derivation

Differential and skid-steer drive are two common robot locomotion models. Both are used extensively in USAR robots. This Chapter presents the assumptions and formulation of the equations for differential and skid steered vehicles. Understanding the assumptions and formulation presented here is important to the development of heterogeneous and heterogeneous differential drive models presented in chapter five and six. Since traditional differential and skid steered models do not fit the actuation regime of resource constrained robots augmented with bulk motive force actuators presented in this thesis, the formulation of heterogeneous and heterogeneous differential drive is needed.

## 3.1 Differential Drive

All differential drive platforms have a configuration similar to the one depicted in Figure 11 and are based on five basic, yet critical assumptions.

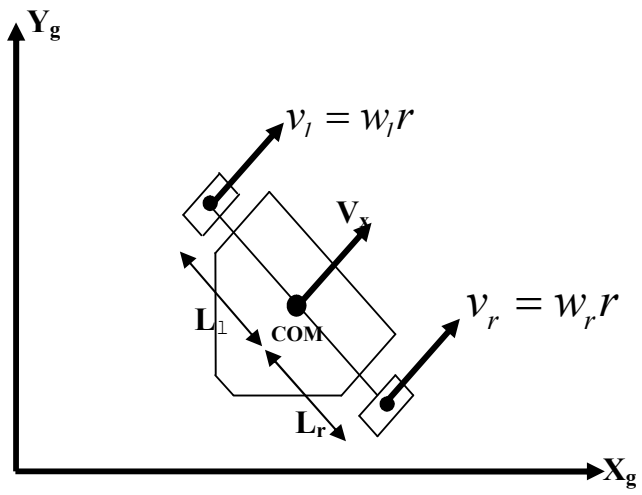


**Figure 11:** Model of differential drive robot

1) The vehicles always consist of two wheels
2) The two wheels are of equal radii; $r$
3) The angular velocities of both wheels can be independently controlled; $w_l$, $w_r$
4) Both wheels always lie on the same axis of rotation
5) Linear and angular velocities; $\dot{\theta}$, $\dot{x}$, $\dot{y}$ are always calculated about the center of mass (COM) which is assumed to always lie on the axis of rotation and always halfway between the two wheels.

The robot depicted in Figure 11 is a planar robot, meaning there are three control variables of interest: $\dot{x}$, $\dot{y}$ representing linear velocity in the plain and $\dot{\theta}$ representing the angular velocity of the robot about the z axis. Figure 12 simplifies and zooms in on the image to define the important variables used in the derivation of the equation for $\dot{\theta}$.

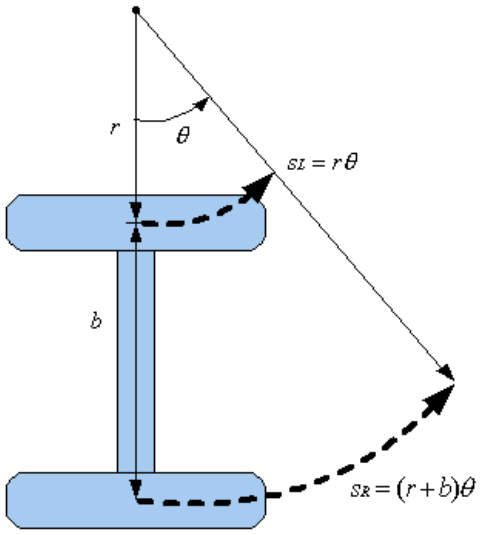


**Figure 12:** Examining change in path length of a differential drive robot

In Figure 12 $SL$ represents the arc length that the left wheel will drive assuming the robot is fixed at an imaginary point $r$ units away from the point of contact of the left wheel. Based on geometry this arc length $SL$ is defined as $r\theta$ where $\theta$ is the angle in radians that is swept. Similarly $SR$ is the arc length that the right wheel will travel and it is equal to

$$SR = (r + b)\theta \qquad (1)$$

where $b$ is the distance between the robot's contact points with the ground or is equivalent to

$$b = L_l + L_r \qquad (2).$$

Taking the time derivative of the change in arc length $SL$ yields

$$\frac{dSL}{dt} = r\dot{\theta} => V_L \qquad (3)$$

and similarly the time derivative of $SR$ yields

$$\frac{dSR}{dt} = (r + b)\dot{\theta} => r\dot{\theta} + b\dot{\theta} => V_R \qquad (4)$$

combining these two equations yields

$$\frac{V_R - V_L}{b} = \dot{\theta} \qquad (5).$$

Deriving the equation for $\dot{x}, \dot{y}$ requires determining the coordinates for the initial (time $T$) position as well as the position obtained after some known time ($\Delta T$). The change in position from $x$ to $x'$ and $y$ to $y'$ (See Figure 13 for clarification) is defined as

$$\frac{dx}{dt} = b(t)\cos\theta \qquad (6)$$

and

$$\frac{dy}{dt} = b(t)\sin\theta \qquad (7).$$

Where is simply the average velocity of the two wheels hence

$$b(t) = \frac{1}{2}(V_R + V_L) \qquad (8).$$

Leading to

$$\dot{x} = \frac{1}{2}(V_R + V_L)\cos\theta \qquad (9)$$

and

$$\dot{y} = \frac{1}{2}(V_R + V_L)\sin\theta \qquad (10).$$

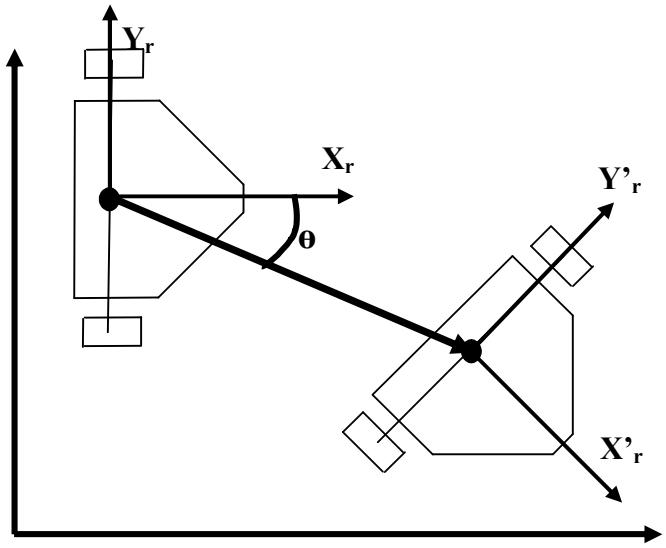


**Figure 13:** Robot Displacement over time for deriving linear velocities

These equations match those found in literature [24,25] and are intuitively pleasing. Take the wheelchair, for example, if both wheels turn at the same angular velocity and hence at the same linear velocity the wheelchair will travel forward in a straight direction. If the wheels turn in opposite directions, the wheelchair will spin in place. Another important observation is that there is zero slip at the wheels or actuation points. This means that there is perfect rolling motion and no velocity component perpendicular to the direction of travel, $V_x$ .

### 3.2 Skid Steer Drive

Skid steered vehicles can be generalized as differential drive vehicles that allow slip along the perpendicular direction of travel.

The skid steered vehicle model requires several assumptions:

1) All actuators are wheels or tracks
2) Wheels are set up as differential pairs
3) Wheels are individually controlled

Skid-steered vehicles are similar to differential drive vehicles, but generally consist of four or more wheels arranged as two or more differential pairs. Some designs of skid-steered vehicles involve a tread wrapping the two wheels on the same side, creating two active surfaces of actuation. Therefore, a skid-steered vehicle generally has two or more points of actuation on each side of the vehicle. Due to the multiple pairs of differentially driven actuators, there is no instant center of rotation that satisfies every pair. As can be seen in Figure 14, slipping must occur for the vehicle to rotate about the pre-described instant center of rotation denoted by vectors $v_{1y}\ v_1 \ldots v_{4y}$, representing the lateral velocities at each contact point. In the case of wheels, lateral velocities mean slip. Once again, a skid-steered vehicle model assumes contact points at the wheels as a single point hence no wheel width is taken into account.

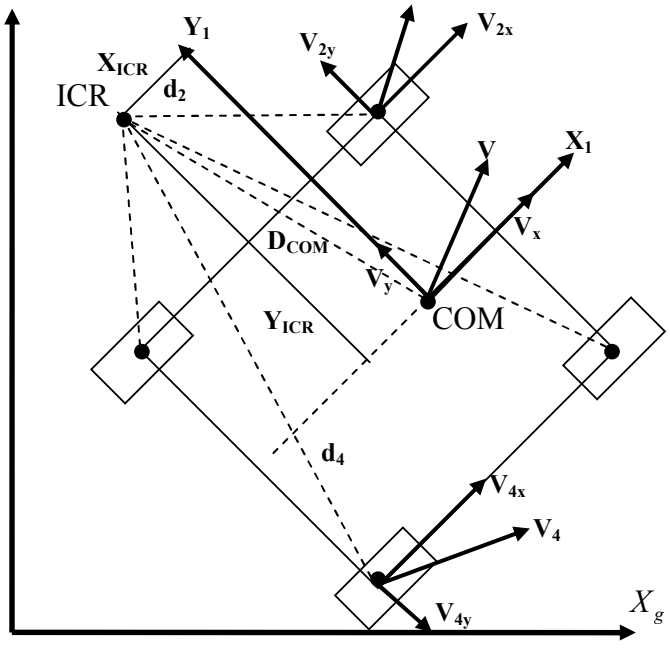


**Figure 14:** Model and associated vectors for skid steered vehicle (modified from [23])

Lengthy explanations, available in literature, [23] derive the equations for skid-steer vehicles. Equation 1 relates lateral and longitudinal velocities of the different points of contact to the linear and angular velocity of the vehicle taken at the center of mass "COM". In Equation 11, $c$ is one half the width of the vehicle, $b$ is as distance from the COM to the front of the vehicle, $a$ is the distance from the COM to the back of the vehicle, $x_{ICR}$ is the measured distance of $d_c$ projected on the $x$ axis of a coordinate frame aligned with that of the vehicle coordinate frame at the ICR. While, $v_L$, $v_R$, $v_F$, $v_b$ are defined according to (12-15). $x_{ICR}$ is an indirect measurement of the radius of curvature the vehicle will follow, and a general form of the measurement is show in 6.

$$\begin{bmatrix} v_L \\ v_R \\ v_F \\ v_b \end{bmatrix} = \begin{bmatrix} 1 & -c \\ 1 & c \\ 0 & -x_{ICR}+b \\ 0 & -x_{ICR}-a \end{bmatrix} \begin{bmatrix} v_x \\ w \end{bmatrix} \tag{11}$$

$$v_L = v_{1x} = v_{2x} \tag{12}$$

$$v_R = v_{3x} = v_{4x} \tag{13}$$

$$v_F = v_{2y} = v_{3y} \tag{14}$$

$$v_B = v_{1y} = v_{4y} \tag{15}$$

$$d_c = \frac{v_x}{w} = \frac{c(v_l + v_v)}{v_r - v_l} \tag{16}$$

As previously explained with differential drive vehicles, the input required in order to command the wheels of a skid steered vehicles is the forward desired linear and angular velocities.

Further analysis in the literature describes the forces and torques imparted at the idealized points of contact due to lateral slip which is a function of friction at those points. This friction must be overcome by the driving actuators in order to provide the

desired linear and angular velocity for the vehicle. The magnitude of the lateral slip is proportional to $x_{ICR}$, which is a measure of the turning radius similar to the differential drive model $k$. When the instant center of rotation is very far away from the robot, $x_{ICR}$ approaches zero, resulting in a turning radius of zero and thus leading the robot in a straight direction. When $x_{ICR}$ is at its maximum value, the robot is rotating in place. At this point, lateral slip velocities are at their maximum and lateral torques and moments. Hence, the friction that must be over come is also at a maximum.

# Chapter 4
# Crabinator

The TerminatorBot, developed previously in our lab group, is a two limbed biologically-inspired, small and resource constrained robot. This Chapter presents Crabinator depicted in Figure 15 as a proposed solution for a bulk motive actuator to augment resource constrained robots such as the TerminatorBot. The Crabinator module [26] builds on the idea that some of the more versatile USAR robots are limbed tracked hybrids. For this reason, the Crabinator module is a single degree of freedom (DOF), tread actuator.

**Figure 15:** Prototype Crabinator module attached to TerminatorBot

The complete tracked limbed, augmented robot, seen in Figure 16, and appears to fit the mold of a differential drive or a skid-steered robot. This Chapter explains the mechanical design of the Crabinator and shows how the new hybrid drive system is not accurately described by either the skid-steered or differential drive models. In subsequent chapters we will introduce a heterogeneous differential drive model and demonstrate how the TerminatorBot augmented with the Crabinator module is an example of such a drive model. This drive model comes from the breaking of the assumptions of differential drive models which will also be presented in subsequent chapters. Additionally, the current chapter presents some of the challenges encountered in the design of the treads and the implementation of the grouser solution. Finally, showing how a proposed method for synchronizing the Crabinator with the TerminatorBot producing the side slipping locomotion desired.

**Figure 16:** TerminatorBot augmented with Crabinator Module

### 4.1 Design of the Crabinator

Since one of the unique attributes of the TerminatorBot is its small size, any modules attached to it are also designed to stay small. The final Crabinator modules consist of one Maxon 1.5W motor instrumented with a 16 count encoder and a 255:1 gear

box. This combination of components yields a motor module that is 13mm in diameter and 55mm in length, capable of both sensing position and providing the torque necessary to drive the motor. The final part of the module is a pinion gear attached to the motor shaft output that directly drives a modified tank tread wrapped around the Crabinator modules, as seen in Figure 15. The tank treads used presented an additional constraint of the design. The treads used are 38mm long, meaning that is the minimum width of the Crabinator module had to be equal or greater then 38mm to maintain support of the tread.

The completed module is 65mm in diameter and roughly 60mm long. This single DOF actuator is capable of slipping over the original TerminatorBot body frame with an overlap of 10mm where four 4-40 screws attach to the TerminatorBot body. The tank treads ride in a countersink cut into the Crabinator body so only the thickness of the tread protrudes about the 65mm diameter. The treads are driven by a pinion gear that is placed in a notch in the body such the tension is kept constant and slip occurs. As can be seen in Figure 17 the motor lies horizontally. An alternative space saving design, shown in Figure 17, was explored where the motor stood vertically.

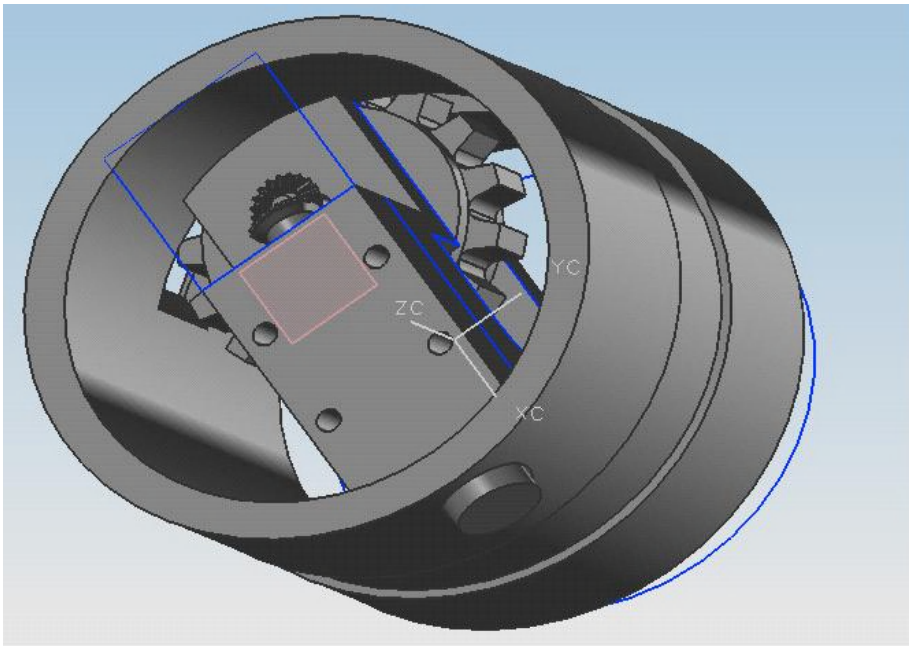


**Figure 17:** Cad drawing of alternative design of Crabinator module

This alternative design was abandoned mainly due to reliability issues. The design required two forty five degree bevel pinion gears to be precisely positioned to connect to the drive gear of the tank treads leading to high failure rates. Additionally this alternative design required more machining time hence cost will eventually become a factor.

The electronics required for the Crabinator modules are a motor driver h-bridge circuit and a small microprocessor to interpret the quadrature encoder on the Maxon motor. Additionally, the microprocessor which in the final design will be onboard interprets the data coming from the arms of the TerminatorBot. Synchronization is critical between the TerminatorBot and Crabinator module. Currently these electronics are connected to the Crabinator modules via a tether. In future versions, all of the electronics will be housed on-board, particularly once the reconfigurable morphing bus FPGA [31] is implemented on the TerminatorBot.

### 4.2 Grousers and Friction

When the TerminatorBot, augmented with the Crabinator modules, locomotes in the longitudinal direction (along the axis of the cylindrical body, Figure 18), the tread contributes insignificantly, and thus remains motionless. The limbs drag the body forward, as occurs when the transverse tread module is not attached.


**Figure 18:** Locomotion direction of TerminatorBot with Crabinator module

However, the prototype tread module illustrated in Figure 18 causes greater friction for forward travel than the smooth body of the robot. This section investigates design efforts to mitigate that negative effect where the actuator module increases available power in the transverse direction, while not impeding locomotion in the longitudinal direction.

To achieve non-isotropic frictional characteristics, tread "shoes" (grousers) are designed based on simple cantilever beams capable of large deflection angles. When the tread motion is in the transverse mode, the beams appear stiff, transmitting the full force of the tread to the ground for power. When locomoting in the longitudinal mode, the

beams appear soft and will bend over, like the bottom of a sled, providing a smooth surface with minimal resistance to motion (Figure 19).

There is considerable research into the longitudinal and transverse frictional behavior of rubber tires gripping a smooth road surface, [32][33] differing from prior formulations in that in this application the transverse and longitudinal motion occurs in two different regimes: slipping and non-slipping. Furthermore, the "rubber" configuration is not that of a single surface contact patch, but a discrete "brush" configuration. In fact, this has many similarities to "sipping" in tire manufacture.

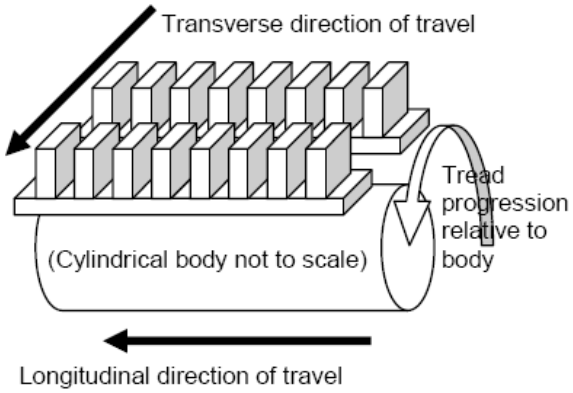


**Figure 19**: Flexible tread "shoe" provides non-isotropic characteristics

### 4.2.1 Grouser Geometry

Achieving appropriate anisotropic traction behavior, while maintaining other performance characteristics, involves a variety of variables. These variables include material properties, system-level configuration, and detailed mechanical design. For this part of the analysis, it is assumed that the system configuration is chosen to include cantilever beams on the tread faces to achieve the anisotropic behavior. Given that, the first step is to investigate the range of materials that provide suitable Young's moduli.

Young's modulus is at the core of modeling cantilever beams and appears in both finite element analysis as well as analytic formulations of beam theory. Silicon rubber, which has a Young's Modulus in the range of 0.01 - 0.1 GPa was decided as the initial material of choice for forming the tank treads. Silicon rubber has many characteristics that make it a natural first choice: liquid uncured state makes it compatible with shape deposition manufacturing [43]; surface finish is somewhat slippery; it is safe; and it is available in a range of durometer.

An Instron Material Testing System (MTS) was used to experimentally determine Young's modulus for samples of different candidate materials. For each material, a circular test coupon was cut from a martial sample provided. The thickness and diameter of the test coupon was recorded then gradually subjected to a compression load of 890N (200lbs). The Instron produces plots of load versus displacement. Each sample was loaded and unloaded five times and a data acquisition system recorded the displacement. Equation 17 is applied to the force/displacement data and the average Young's modulus (E) for each sample appears in Table 1.

$$\mathrm{E} \equiv \frac{\text{tensile stress}}{\text{tensile strain}} = \frac{\sigma}{\varepsilon} = \frac{F / A_0}{\Delta L / L_0} = \frac{F L_0}{A_0 \Delta L} \qquad (17)$$

**Table 1:** Experimental Young's Modulus for Several Samples

| All units in Pascals | Smooth-Sil 930 | Reoflex30 | DragonSkin | ecoflex 5 |
|---|---|---|---|---|
| Set 1 | 2.08E+06 | 1.22E+06 | 9.79E+05 | 1.15E+06 |
| Set 2 | 1.83E+09 | 1.20E+06 | 9.90E+05 | 1.09E+06 |
| Set 3 | 1.76E+06 | 1.18E+06 | 9.45E+05 | 1.07E+06 |
| Set 4 | 1.82E+06 | 1.18E+06 | 9.41E+05 | 1.05E+06 |
| Set 5 | 2.00E+06 | 1.16E+06 | 9.38E+05 | 1.08E+06 |
| | | | | |
| average | 1.92E+06 | 1.19E+06 | 9.59E+05 | 1.09E+06 |
| stdev | 151114 | 22775 | 23821 | 37486 |

The fundamental approach is to use a non-isomorphic cantilever beam design to achieve the anisotropic behavior desired. A rectangular cantilever beam, for example, is profoundly stiffer in the long dimension than in the short dimension. Cantilever beam stress/strain computations, which are covered in many undergraduate texts, determine deflection angle and tip displacement. For cantilever beams with rectangular cross sections, this is calculated by simply differentiating (18) for load four times, where $E$ is the Young's modulus of the material and $I$ is the second moment of inertia for the cross section of interest [34].

$$load = \frac{dv}{dx} = EI\frac{d^4y}{dx^4} \qquad (18)$$

Equation 18 and the subsequent derivatives make the assumption that the tip displacements are very small with respect to beam dimensions. Since this design is based on large deformations of the beams (an appreciable change in geometry to create the sled-like surface is desired) small-displacement beam theory only as a good starting point for determining reasonable non-isomorphic geometries. Small-displacement beam theory only considers perpendicular forces and does not take into account parallel loads or buckling, which the beams in this design experience in practice. Using small displacement gave a good starting point for the experiment.

For a rectangular cantilever beam as shown in Figure 20 the rectangular cross section stays uniform along the L direction. Therefore, $I$ is constant at $bh^3/12$ when applying F1 (longitudinal direction of travel) or $b^3h/12$ when applying F2 (transverse direction of travel). Using the derivatives from (18), Matlab was utilized to solve the

basic beam equation with the second moment of inertia parameters above, a preliminary set of non-tapering beams was created (Figure 21) with dimensions L = 6.4mm, $h$ = 3.2mm, $b$ = 8.3mm.

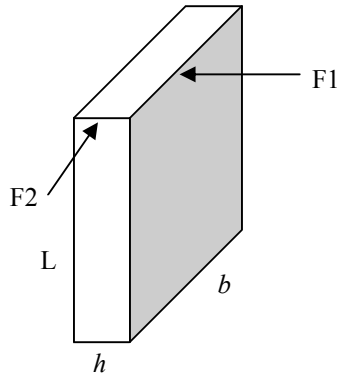


**Figure 20:** Rectangular cantilever beam

Qualitatively, these beams felt a little too stiff and did not have the desired bending curve for the non-isotropic behavior. A trapezoidal beam should result in a diminishing radius curve, producing a sled-like surface to rubble.

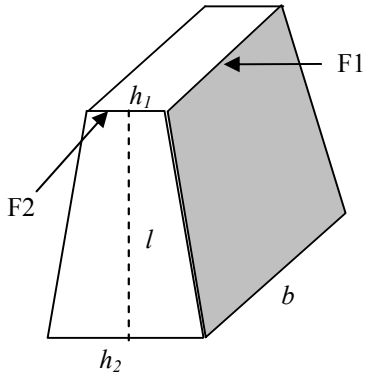


**Figure 21:** Trapezoidal cantilever beam

With a trapezoidal cantilever beam as shown in figure 21, the cross section is also rectangular therefore, the second moment of inertia has the same form of either $bh^3/12$ or $b^3h/12$. But, as can be seen in Figure 21, $h$ varies along the $l$ direction. To account for that

the new second moment of inertias for F1 and F2, that must be integrated for times are (19) and (20) for F1 and F2 respectively.

$$I_{F1} = \frac{b(h_2 + (h_1 - h_2)\frac{x}{l})^3}{12} \qquad (19)$$

$$I_{F2} = \frac{b^3(h_2 + (h_1 - h_2)\frac{x}{l})}{12} \qquad (20)$$

Performing the integration using Matlab once again, the new prototype geometry becomes: $l$ = 6.4mm, $h_2$ = 4.8mm, $h_1$ = 1.0mm, $b$ = 8.3mm

### 4.2.2 Grouse Testing

In order to test the prototype treads shown in Figure 22 and Figure 23, the experimental setup shown in Figure 24 was used. The tread in Figure 22 is a uniform tread of SmoothSil 930 silicone rubber. The tread in Figure 23 is a multi-material shape deposition manufactured tread with a core of SmoothSil 930 and an external layer of Forsch 680 urethane with smoother finish to increase slip. The third tread (not pictured) is a uniform core of Forsch 680.

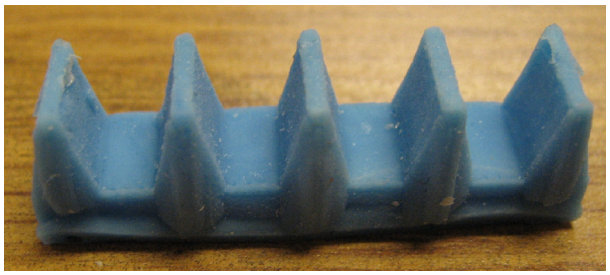

**Figure 22:** Solid SmoothSil 930 tread. (25mm in length.)

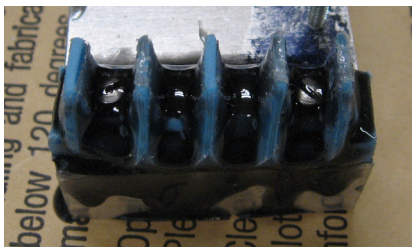

**Figure 23:** SmoothSil930 tread with Forsch 680A urethane deposited on the surface

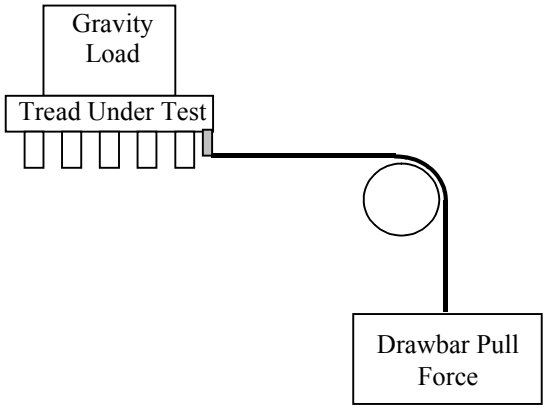


**Figure 24:** Experimental setup

In this setup, a rectangular aluminum sled was created onto which two sets of treads are attached. Atop the sled a 300, 200, or 100-gram weight is attached so the net gravity load is 410, 310, or 210 grams. (410 grams is close to the current prototype load at the back of the TerminatorBot with the Crabinator unit attached.) To the bottom of the sled a screw is attached to which a string is attached. This screw is adjusted so the string is as low as possible to prevent tipping and uneven loads on the cantilever beams. This string is connected to a cup to which weight is gradually added until static coefficient is broken and the sled moves with constant velocity, thus balancing dynamic friction. (Dithering or tapping the sled is helpful to find the dynamic coefficient.) This force is recorded for both longitudinal and transverse orientation of the treads. Multiple trials are recorded and a median value is determined and presented Table 2.

**Table 2:** Frictional Forces on a Smooth Surface with 410 Gram Load

| **Tread Type** | **Transverse Friction (g)** | **Longitudinal Friction (g)** |
|---|---|---|
| SmoothSil 930 | 250 | 300 |
| Forsch 680 | 220 | 240 |
| 930/680 Combo | 230 | 300 |

In every case, the collapsing tread actually goes up in total friction. This is not too surprising for smooth surfaces, as in the above tests, because the total surface area goes up when the tread collapses. As expected, there are clear differences between materials. The Forsch 680, a polyurethane, produces the smallest increase between transverse and longitudinal directions, despite the increase in surface area.

Urban search and rescue environments are not smooth surfaces. To simulate the effects of gearing friction in a rough environment in a standardized way, we tested the grousers on regular step fields, as shown in Figure 25. Using step heights of 0.0, 0.1, 2.0, 2.3 mm. Furthermore, a surface material with slightly higher coefficient of friction was used.

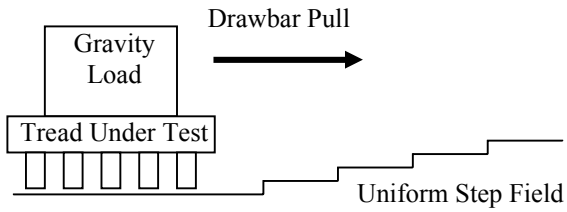


**Figure 25:** Uniform step field tests to simulate gearing friction in rough/uneven environments.

**Table 3:** Frictional Forces on a Stepped Surface

| Tread Type | Load (g) | Step (mm) | Trans. Frict. (g) | Long. Frict. (g) | Ratio Long/Trans |
|---|---|---|---|---|---|
| S930 | 410 | 0.0 | 358 | 500 | 1.40 |
| F680 | 410 | 0.0 | 181 | 158 | 0.88 |
| S930 | 310 | 0.0 | 258 | 358 | 1.39 |
| F680 | 310 | 0.0 | * | * | |
| S930 | 210 | 0.1 | 258 | 304 | 1.18 |
| F680 | 210 | 0.1 | * | * | |
| S930 | 410 | 0.1 | * | * | |
| F680 | 410 | 0.1 | 258 | 230 | 0.89 |
| S930 | 210 | 2.0 | 385 | 235 | 0.61 |
| F680 | 210 | 2.0 | 808 | 485 | 0.60 |
| S930 | 310 | 2.0 | 458 | 308 | 0.67 |
| F680 | 310 | 2.0 | * | 558 | |
| S930 | 210 | 2.3 | 408 | 258 | 0.63 |
| F680 | 210 | 2.3 | 1035 | 708 | 0.68 |
| S930 | 310 | 2.3 | 508 | 335 | 0.66 |

From Table 3 we see that, for nearly every step size and load, the ratio of longitudinal friction to transverse friction is less than 1.0. This means that the cantilever beam grousers are, in fact, reducing the resistance to longitudinal motion while providing significant traction for transverse motion.

### 4.3 Crabinator TerminatorBot Synchronization

The present section examines how the Crabinator module is synchronized with the TerminatorBot to produce a heterogeneous differential drive mechanism. As seen in chapter three, command of the velocities of the left and right ‘wheels’ are required to drive a differential drive robot. Although the TerminatorBot augmented with the Crabinator drive module is not exactly a differential drive robot similar commands are necessary. In the case of the TerminatorBot augmented with the Crabinator that means commanding both the arms of the TerminatorBot and the tread velocity of the Crabinator. For pure transverse or side slipping locomotion, a master-slave regime is implemented to

maintain unity between net transverse wheel velocity and arms velocity. Therefore, the ratio between the master-TerminatorBot and slave-Crabinator is one causing the robot to move parallel to the transverse direction. To achieve rotation about the center of mass as seen by the equations in chapter three requires that the ratio between the master and slave is not one hence a non-unity master slave relationship is applied.

### 4.3.1 Master Slave Details

In the case of augmented robot described in this chapter, the TerminatorBot's arms are treated as masters and the Crabinator tank tread as slave. This is achieved by computing the forward kinematics of one of the arms through a shift left gait of the arms. The forward kinematics provided the X, Y, Z position of the tip relative to center point between the two arms as shown in Figure 26.

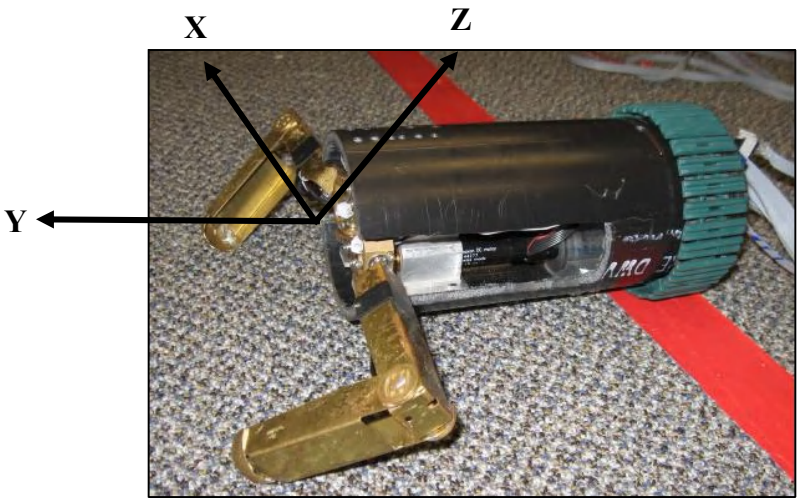


**Figure 26:** Reference frame for translation on TerminatorBot augmented with Crabinator module

Relative to the coordinate system picked for the TerminatorBot, translation in the X direction is considered "side slipping." Arm velocity is calculated by taking the

derivative of the X position. This can also be determined via the Jacobian of the arm. To complete the synchronization, the Crabinator module only needs to match the arm velocities with the wheel velocities. One important note is that the Crabinator module must only match velocities in the X direction when the arms are actually in contact with the ground (i.e., while the TerminatorBot center of mass is translating). The shift left gait consists of four phases. Assuming the first position to be the "goal post" position where both arms are bent 90 degrees at the elbow and are parallel to the ground, like a football goal post. The first phase is moving both arms from the goal post to the left or right to directly above where they will contact the ground. The second phase consists of lowering them to the ground and raising the TerminatorBot's body. The third phase involves the actual shift of the TerminatorBot to the left while the arms move to the right. The fourth phase raises the arms from the ground and moves them back to the initial goal post position. It is important to note that while phases two, three and four include changes in the X position of the arms, only in phase three does the body actually move. At this point in phase three, the Crabinator module must be activated to achieve the desired sideways locomotion. Therefore, only during the third phase is the X position of the arm transmitted to the Crabinator modules, where inverse kinematics are performed and the arms synchronize with the treads for unity master slave relationship.

In order to achieve rotation about its center of mass of the TerminatorBot augmented with the Crabinator, different velocities must be commanded according to the equations in chapter three. This can be achieved by using the master slave relationship only this time the ratio is not one and hence before computing the wheel velocity of the

Crabinator this ratio must be pre-multiplied to achieve the desired velocity. If the value is negative, the wheel must rotate in the opposite direction.

# Chapter 5:
# Formulation of Heterogeneous Differential and Heterogeneous drive

As research into more novel locomotion methods continues, advanced robot drive systems will evolve that violate the assumptions made in the formulation of skid steered and differential drive models. The TerminatorBot augmented with the Crabinator module is an example of a robot that violates these assumptions. Augmenting the TerminatorBot with the Crabinator drive module created a robot that appears similar to a differential drive robot. The Crabinator side could be considered half of a differential drive or half of a skid steered robot yet the arm side do not fit the assumptions of differential drive or skid steered robots. This chapter analyzes the violated assumptions in the differential and skid steered drive models and proposes a new heterogeneous differential drive model providing a more general control method..

## 5.1 What is Heterogeneous Differential Drive?

Heterogeneous differential drive fills the gap between traditional differential drive and skid steered vehicles. This theoretical class of vehicles lies in the gray area between pure differential drive vehicles and pure skid steered vehicles, yet represents both at the extremes. Heterogeneous differential drive also provides the basis for preliminary development of the heterogeneous drive as a more general class of heterogeneous

differential drive vehicles. Heterogeneous differential drive vehicles are those with only two actuation points of contact with the ground while heterogeneous drive vehicles are considered as multi ground contact vehicles.

Heterogeneous differential drive relaxes some of the symmetry assumptions of traditional differential drive. Consider Figure 27, illustrating a trivial extension to include wheel-like points of contact that lie on a line with the center of mass, but are not equidistant. In the TerminatorBot augmented with the Crabinator this extension is true because the COM lies near the front where the arm. The four drive motors are located near the arms hence shifting the COM away from the center. Two key points illustrated in this figure are that $L_l$ and $L_r$ are of different length. Other important point is that the reference frame designated with prime is the reference frame of the COM and the non primed reference frame is where the general differential drive model equation are derived from, meaning that $L_l$ and $L_r$ are of equal length.

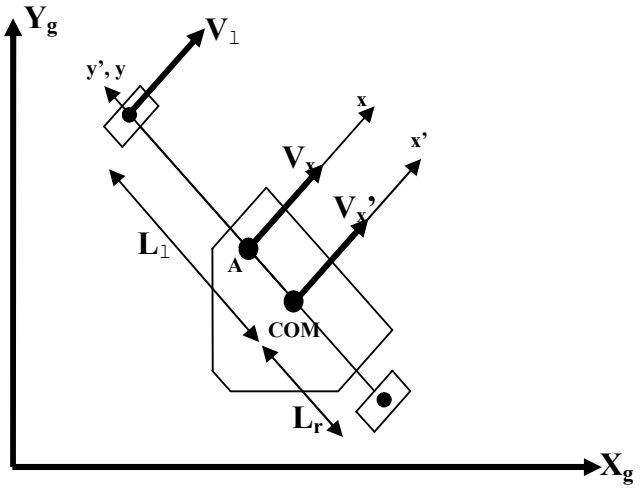


**Figure 27:** Differential drive vehicle with asymmetric actuators and offset COM

For reference equation 20 below combines equations 5,9,10 from chapter 3 into a general form equation describing motion of a differential drive robot in the global frame as a function of input velocities $v_l$ and $v_r$. In equation 20 $L$ is equivalent to $b$ which is equivalent to $L_l + L_r$ in Figure 17.

$$\begin{bmatrix} \dot{X} \\ \dot{Y} \\ \dot{\theta} \end{bmatrix} = \begin{bmatrix} -\frac{r}{2}\cos\theta & -\frac{r}{2}\cos\theta \\ -\frac{r}{2}\sin\theta & -\frac{r}{2}\sin\theta \\ \frac{r}{L} & -\frac{r}{L} \end{bmatrix} \begin{bmatrix} v_l \\ v_r \end{bmatrix} \qquad (20)$$

Equation 21 describes motion of the robot frame as a function input velocities.

$$\begin{bmatrix} 1 & 0 & b/2 \\ 1 & 0 & -b/2 \end{bmatrix} \begin{bmatrix} v_x \\ v_y \\ \omega \end{bmatrix} = \begin{bmatrix} v_l \\ v_r \end{bmatrix} \qquad (21)$$

An important note to make about equation 21 is that the assumption of differential drive that $v_y$ is zero is kept.

To describe the motion of the COM of the configuration shown in Figure 27 two additional equations must be derived, the relationship of the COM frame to the global frame which is

$$\begin{bmatrix} \dot{X} \\ \dot{Y} \\ \dot{\theta} \end{bmatrix} = \begin{bmatrix} \cos\theta & -\sin\theta & 0 \\ \sin\theta & \cos\theta & 0 \\ 0 & 0 & 1 \end{bmatrix} \begin{bmatrix} v_x \\ v_y \\ \omega \end{bmatrix} \qquad (22).$$

It must be noted that equation 22 holds true for both the transformation from the primed frame and non-primed frame to the global frame. The second equation that is required is the relationship between the primed and non-primed frame which is

$$\begin{bmatrix} v_x' \\ v_y' \\ \omega' \end{bmatrix} = \begin{bmatrix} 1 & 0 & \frac{L_l + L_r}{2} \\ 0 & 1 & 0 \\ 0 & 0 & 1 \end{bmatrix} \begin{bmatrix} v_x \\ v_y \\ \omega \end{bmatrix} \qquad (23).$$

Using equations 21, 22, and 23 it is now possible to formulate the equation relating the motion of the COM of the robot configuration shown in Figure 27 to $v_l$ and $v_r$. To accomplish this equation 21 must be re-written as

$$\begin{bmatrix} v_x' \\ v_y' \\ \omega' \end{bmatrix} = \begin{bmatrix} \frac{L_l}{L_l + L_r} & \frac{L_r}{L_l + L_r} \\ 0 & 0 \\ \frac{-1}{L_l + L_r} & \frac{1}{L_l + L_r} \end{bmatrix} \begin{bmatrix} v_l \\ v_r \end{bmatrix} \qquad (24).$$

Then taking equation 24 and substituting it into equation 21 and taking the result of that equation and substituting into equation 22 yields

$$\begin{bmatrix} \dot{X} \\ \dot{Y} \\ \dot{\theta} \end{bmatrix} = \begin{bmatrix} \frac{-b_l}{b_l + b_r}\cos\theta & \frac{-b_r}{b_l + b_r}\cos\theta \\ \frac{-b_l}{b_l + b_r}\sin\theta & \frac{-b_r}{b_l + b_r}\sin\theta \\ \frac{1}{b_l + b_r} & \frac{-1}{b_l + b_r} \end{bmatrix} \begin{bmatrix} v_l \\ v_r \end{bmatrix} \qquad (25).$$

The next assumption to be relaxed in going towards a heterogeneous differential drive model is illustrated in Figure 28 where an additional offset $c$ from the center of mass is introduced.

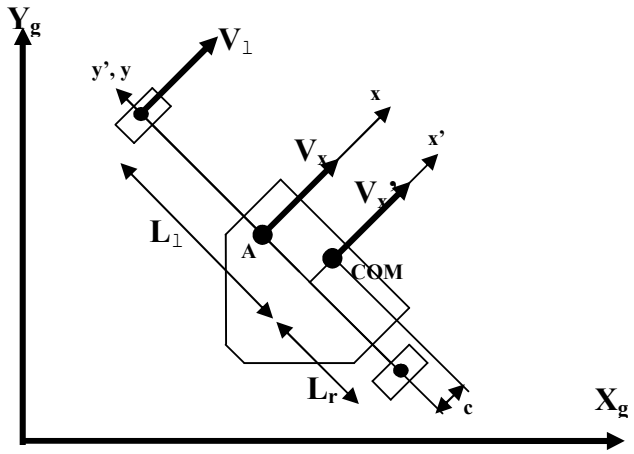


**Figure 28:** Differential drive robot with the assumption that the COM lies on the axis of rotation relaxed

A similar calculation to the one before is performed to derive the relationship for the motion of COM in the global reference frame and $v_l$ and $v_r$. The one additional relationship that is needed is again the transformation between the primed and non-primed frame which is

$$\begin{bmatrix} v_x' \\ v_y' \\ \omega' \end{bmatrix} = \begin{bmatrix} 1 & 0 & \frac{L_l + L_r}{2} \\ 0 & 1 & c \\ 0 & 0 & 1 \end{bmatrix} \begin{bmatrix} v_x \\ v_y \\ \omega \end{bmatrix} \qquad (25).$$

Then taking the inverse of the equation 25 and keeping the assumption that $v_y$ is zero results in the desired equation of

$$\begin{bmatrix} \dot{X} \\ \dot{Y} \\ \dot{\theta} \end{bmatrix} = \begin{bmatrix} \frac{-b_l}{L}\cos\theta - \frac{c}{L}\sin\theta & \frac{-b_r}{L}\cos\theta - \frac{c}{L}\sin\theta \\ \frac{-b_l}{L}\sin\theta - \frac{c}{L}\cos\theta & \frac{-b_r}{L}\sin\theta - \frac{c}{L}\cos\theta \\ \frac{1}{L} & -\frac{1}{L} \end{bmatrix} \begin{bmatrix} v_l \\ v_r \end{bmatrix} \quad (26)$$

Where $L$ is equal to $L_l + L_r$.

The next assumption relaxed that the two drive wheels are not on the same drive axis. It is interesting that when one of the contact points appears at an offset, d, along the x axis of the robot reference frame, as in Figure 29.

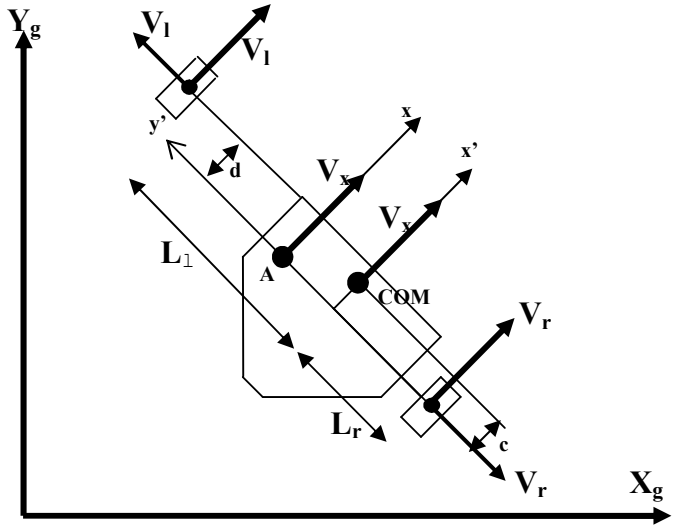


**Figure 29**: A heterogeneous differential drive robot model with the COM offset and the actuators offset

Deriving this most general case follows the same procedure as before where the only difficult part is the transformation matrix and its inverse which are 27 and 28 below.

$$\begin{bmatrix} -1 & \frac{2L}{2c-d} & -L_l \\ -1 & \frac{-2L}{2c-d} & L_r \end{bmatrix} \tag{27}$$

$$\begin{bmatrix} \frac{L_l}{L} & -\frac{L_r}{L} \\ \frac{2c-d}{2L} & \frac{-(2c-d)}{2L} \\ \frac{1}{L} & -\frac{1}{L} \end{bmatrix} \tag{28}$$

The resulting equation when substituting equation 28 as before into equations 21 and 22 yields

$$\begin{bmatrix} \dot{X} \\ \dot{Y} \\ \dot{\theta} \end{bmatrix} = \begin{bmatrix} \frac{-b_l}{L}\cos\theta - \frac{2c-d}{2L}\sin\theta & \frac{-b_r}{L}\cos\theta + \frac{2c-d}{2L}\sin\theta \\ \frac{-b_l}{L}\sin\theta + \frac{2c-d}{2L}\cos\theta & \frac{-b_r}{L}\sin\theta - \frac{2c-d}{2L}\cos\theta \\ \frac{1}{L} & -\frac{1}{L} \end{bmatrix} \begin{bmatrix} v_l \\ v_r \end{bmatrix} \tag{29}$$

Clearly, this formulation subsumes the traditional differential drive if d=0, c=0, and $L_l$ = L. See Figure 30.

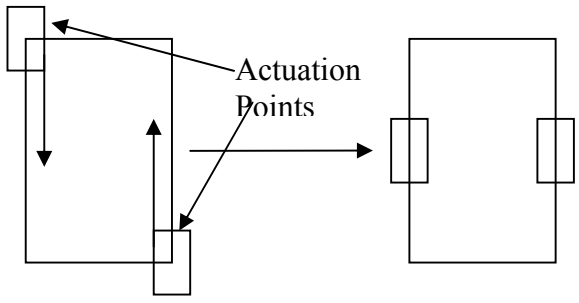


**Figure 30:** The heterogeneous differential drive mechanism, left, subsumes the classical differential drive mechanism, right, as the offset approaches zero

However, with the contact points offset in both x and y and exerting velocities only in the x direction, side-slipping of the contact points can occur. Hence equation 30 below relates $v_l$, $v_r$, $v_{ly}$ and $v_{ry}$ to the motion at the body reference frame $v_x$, $v_y$ and $\omega$. Where $v_{ly}$ and $v_{ry}$ represent the side slipping potential of the wheels or more generally actuation points.

$$\begin{bmatrix} v_l \\ v_r \\ v_{ly} \\ v_{ry} \end{bmatrix} = \begin{bmatrix} -1 & \frac{2L}{2c-d} & -b_l \\ -1 & -\frac{2L}{2c-d} & b_r \\ 0 & -\frac{2d}{2c-d} & \frac{d}{2} \\ 0 & \frac{2d}{2c-d} & -\frac{d}{2} \end{bmatrix} \begin{bmatrix} v_x \\ v_y \\ \omega \end{bmatrix} \qquad (30)$$

**5.2 Heterogeneous Drive**

The heterogeneous differential drive model presented is still limited because it requires two actuation points on different halves of the robot. It is desirable to develop a more general model that can apply to all bulk motive actuators. This model that is presented here is heterogeneous drive. The ground work presented here for heterogeneous drive encompasses drive mechanisms that are generally asymmetric in form and asymmetric in means of actuation. This includes, for example, the Crabinator which falls under heterogeneous differential drive. Additionally it will include impulsive drive robots such at the TerminatorBot augmented with the active tether impulse module [40], explained in greater detail in chapters six, or a two dimensional tread module [40].

### 5.2.1 Example of Heterogeneous Drive

One of the primary interests of this thesis is heterogeneous drive vehicles – vehicles that have little or no symmetry in their drive train. An example of this type of vehicle is the water hammer actuated TerminatorBot robot, illustrated schematically in Figure 31 [27]

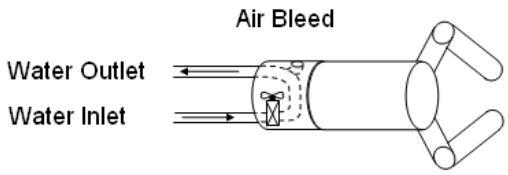


**Figure 31**: Water hammer actuator with TerminatorBot forming a heterogeneous drive robot

In this type of vehicle, the arms are the primary mode of actuation and steering and they operate independently at two points of contact to drag the robot forward. The water hammer actuator is a form of active tether that imparts a series of impulsive forces on the back of the robot to propel it forward. These impulsive forces result from the momentum transfer as fluid flowing in the tether is abruptly stopped by the valve.

From an analysis standpoint, this robot is certainly not an Ackerman-steered vehicle and it is neither skid steered nor differential drive. Yet, the coordination of the multiple contact points (heterogeneous drive vehicles must have a minimum of two actuation points and actuation means) creates problems similar to the heterogeneous differential drive: the points of contact may not be precisely controllable with respect to their lines of action and with respect to induced motion. While this work is still preliminary, chapter four showed a generic framework for channeling these forces by computing the derivative of the velocities from the heterogeneous differential drive

formulation (expanded for n points of contact) and using the multi-body dynamics of the entire robot to relate accelerations and forces. By deliberately shaping non-isotropic properties of the mass matrix through the manipulator configuration space, whole-body steering of the robot can be accomplished. A preliminary example will be explained below.

In the TerminatorBot augmented with a water hammer [26], [27] active tether, the water hammer action imparts a force on the robot which accelerates the robot. Since the direction from which the water hammer imparts force is fixed (this assumption can be relaxed in the future if deemed necessary) as assumed in [26], this means that the arms must some how be commanded. As stated previously, by taking the derivatives of $v_x'$, $v_y'$, $w'$ one can now look at F = MA. In this case, A is a column vector consisting of $\dot{v}_x'$, $\dot{v}_y'$ and $\dot{w}'$ representing desired linear and angular velocities of the center of mass. The force vector F for the time being is fixed as an input vector due to the assumption that the impulsive forces are coming from a fixed direction. This means in order to control the acceleration M must be manipulated and M is a function of the body's configuration.

In order to control the mass matrix of the vehicle, whole body dynamics of the vehicle must be computed. In previous work on mass matrix control, [28] this was achieved using the Operational Space formulation of Khatib [29]. In this work the assumption of slow velocities and planer motion where made which are consistent with the assumptions made in the formulation of the equation for skid steered vehicles. The conclusions from the mass matrix work are summarized in 29-30 where $\Lambda(x)$ is the

augmented mass matrix of vehicle. Hence by manipulating the vehicle mass matrix, described in [30] and knowing the desired forces on the body which is the input vector, it is possible to control the accelerations of the vehicle.

$$\Lambda(x)\ddot{x} = F \qquad (31)$$

$$\Lambda(x)^{-1} F = \ddot{x} \qquad (32)$$

# Chapter 6
# Mass Matrix Control of Heterogeneous Drive Robot

This Chapter will discuss the formulation of a control method of a heterogeneous drive robot and how it can be used with a theoretical impulsive drive method. Operational space and the augmented method [29, 35, 36] are used to develop a non-isotropic Cartesian mass matrix for a robot that is modulated to passively steer the acceleration resulting from a bulk motive force module such as the water hammer.

## 6.1 Previous work

The effective mass of any mechanism in six- space is a six-by-six matrix that can be derived using a variety of methods. One popular approach is the Recursive Newton Euler (RNE) method [37] which produces a motion governing equation (33).

$$A(q)\ddot{q} + b(q,\dot{q}) + g(q) = F \qquad (33)$$

$A(q)$, $b(q,\dot{q})$, and $g(q)$ represent the kinetic energy/mass matrix, Coriolis and centrifugal, and gravitational forces in joint space, respectively. Given the positions, velocities, and accelerations of all the joints, (33) computes the resulting end effector forces and joint torques required to produce the motion.

RNE is a straightforward method to derive (33) for serial chain manipulators. Deriving the same equations for parallel chain manipulators is very difficult because it

requires both forward and inverse kinematics, which can lead to indeterminacy. The Operational Space formulation [29], in conjunction with the augmented object method [35], provides a convenient way to handle parallel-chain configurations by decomposing the system into multiple serial chains. The operational space method solves for forces and torques at an "operational point" that is chosen for convenience. This operational point is in Cartesian space, so the governing equation becomes:

$$\Lambda(x)\ddot{x} + \upsilon(x,\dot{x}) + p(x) = F \qquad (34)$$

Since equation, (34) is written in operational space, the kinetic energy/mass matrix, Coriolis /centrifugal and gravitational forces must be formulated in Cartesian space as opposed to joint space. The relationship between the operational space and joint space mass matrices appears in (35) where $J$ is the Jacobean in joint space taken at the operational point.

$$\Lambda(x) = J^{-T}(q)A(q)J^{-1}(q) \qquad (35)$$

The key to understanding operational space formulation is the concept of the operational point. The operational point is the point on the object being manipulated by a mechanism, where force control is required. An example of this is an assembly line robot gripping a bolt. The operational point in this case is the Center of Mass (COM) of the bolt. Hence using Operational space allows for a way of describing the joint position, velocities and accelerations needed to impose a desired force on the bolt and not the end effector, which is what RNE solves force for.

The augmented object method uses the concepts of operational space to decouple the mechanism/robot from the load/object it is manipulating. Additionally if multiple

manipulators are grasping/manipulating a single object their mass, Coriolis/centrifugal forces can be individually summed as shown in equations 36-38.

$$\Lambda(x) = \Lambda_{obj} + \sum_{i=1,\ldots,N} C^T{}_i \Lambda_i C_i \tag{36}$$

$$\upsilon(x, \dot{x}) = \upsilon_{obj} + \sum_{i=1,\ldots,N} C_i^T + C_i \upsilon_i \tag{37}$$

$$p(x) = p_{obj} + \sum_{i=1,\ldots,n} C_i^T p_i \tag{38}$$

Where C is a connectivity matrix between the individual objects of the system, and $\Lambda_{obj}$, $\upsilon_{obj}$ and $p_{obj}$ are the kinetic/mass matrix, Coriolis/centrifugal and gravitational forces components associated with the load and are dependent on the load geometry.

### 6.2 Derivation of Heterogeneous Drive Robot Model Based on TerminatorBot

The TerminatorBot locomotes using two arms, each with three degrees of freedom (DOF), by "grasping" the ground and pulling its cylindrical body forward as shown in Figure 32.

**Figure 32:** TerminatorBot in grasping mode

When the arms of the TerminatorBot are engaging the ground, they can be seen as serial link manipulators fixed in a common inertial frame grasping the body of the robot. A grasping robot is a parallel-chain manipulator, which, as stated earlier, presents a difficult example for computation of the mass matrix. For this reason the augmented object method is used to determine the effective mass matrix of the TerminatorBot which allows the channeling of impulsive forces from the water hammer active tether or any other impulsive force module in a controlled manner.

To calculate the system's mass matrix The TerminatorBot is first decomposed into three components: two arms and a body (Figure 33). Each arm is composed of a two-link serial chain with five revolute joints (Figure 34). All bodies are modeled as rectangular solids.

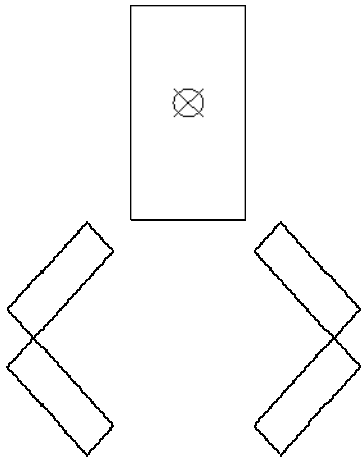

**Figure 33:** Decomposed TerminatorBot

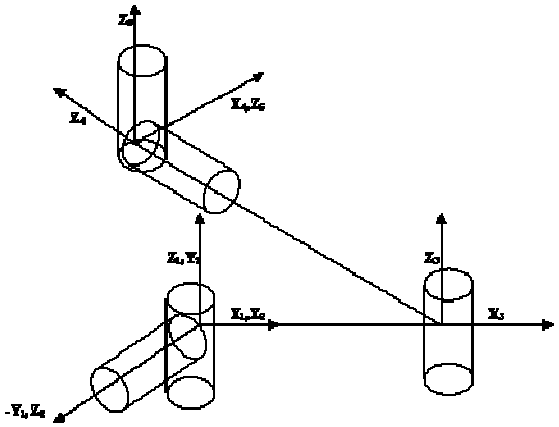

**Figure 34:** Joint orientation of one of the decoupled TerminatorBot arms

In Figure 34, the first two joints are passive and represent the rolling ground contact. Joint 3 is the elbow and joints four and five are the two joints in the shoulder. Table 4 summarizes the DH parameters used in Figure 34 and used in the derivation of the kinematics.

**Table 4**: DH Table for 1 arm of TerminatorBot

| I | $\alpha_{i-1}$ | $a_{i-1}$ | $d_i$ | $\Theta_i$ |
|---|---|---|---|---|
| 1 | 0 | 0 | 0 | $\Theta_1$ |
| 2 | $\Pi/2$ | 0 | 0 | $\Theta_2$ |
| 3 | $-\Pi/2$ | l2 | 0 | $\Theta_3$ |
| 4 | $-\Pi/2$ | 0 | L3 | $\Theta_4$ |
| 5 | $\Pi/2$ | 0 | 0 | $\Theta_5$ |

The third component in the model is the TerminatorBot body. The operational point is chosen as the COM of this body. In general, the operational point can be arbitrarily chosen, but it must remain consistent throughout the derivation.

In order to solve for the possible accelerations of the TerminatorBot's COM, several assumptions have been made:

1) All joints behave as free-swinging passive joints
2) Both tips of the TerminatorBot limbs are firmly affixed to the ground. (The two passive joints allow for rolling motion about the fixed point.)

3) All rigid bodies in the robot are rectangular solids with homogenous mass distribution. All inertial matrixes about the Center of Mass (COM) have the form of Figure 35, where l, w, and h always lay along x,y and z respectively.

$$\begin{bmatrix} \frac{m}{12}(w^2+h^2) & 0 & 0 \\ 0 & \frac{m}{12}(l^2+h^2) & 0 \\ 0 & 0 & \frac{m}{12}(l^2+w^2) \end{bmatrix}$$

**Figure 35:** Inertial Tensor

4) All velocities and accelerations are assumed small and negligible, leading to

$$\Lambda(x)\ddot{x} + p(x) = F \qquad (39)$$

5) The robot is assumed to be resting on the ground therefore, gravitational forces are neglected as in

$$\Lambda(x)\ddot{x} = F \qquad (40)$$

6) Operational point is the COM of TerminatorBot

The form of $\Lambda_{obj}$ is shown in Figure 35

$$\begin{bmatrix} mTbot & 0 & 0 & 0 & 0 & 0 \\ 0 & mTbot & 0 & 0 & 0 & 0 \\ 0 & 0 & mTbot & 0 & 0 & 0 \\ 0 & 0 & 0 & \frac{m}{12}(w^2+h^2) & 0 & 0 \\ 0 & 0 & 0 & 0 & \frac{m}{12}(l^2+h^2) & 0 \\ 0 & 0 & 0 & 0 & 0 & \frac{m}{12}(l^2+w^2) \end{bmatrix}$$

**Figure 36:** Form of $\Lambda_{obj}$

To derive $\Lambda_i$ for each arm, RNE is performed using DH parameters from Table 4 and the inertial matrix for each link shown in Figure 35. The resulting mass matrix is transformed from joint space to operational space using (35). Then the individual

components are summed together using (36). Finally, (40) is rewritten in the following form:

$$\Lambda(x)^{-1} F = \ddot{x} \qquad (41)$$

Based on equation nine it is possible to see that for a heterogeneous drive robot to achieve the desired linear and angular acceleration of the COM manipulation of the mass matrix is required. In the case of the TerminatorBot augmented with a bulk motive actuator this is done by controlling the position of the arms, while for other heterogeneous drive robots it could mean shifting weight around or other innovative solutions for manipulating the mass matrix. Since $\Lambda(x)^{-1}$ is symbolically complex and expensive to compute; only discrete values are calculated and presented in the results section. The results section also shows the results from a simplified planar case containing just one arm and the TerminatorBot body.

### 6.3 Results

#### 6.3.1 Simulation Results of One Arm, One Body

Using Matlab, I employed a discrete, (this Matlab code is available in appendix A) uniform sampling of the robot's configuration space to develop a mapping from configuration space to "acceleration space." Acceleration space is the vector space representing the non-isotropicity of the mass matrix. It represents the instantaneous direction and magnitude of the acceleration of the operational point given a unit force impulse. For the sake of visualization, we present both the one-arm and two-arm planar cases here.

In the planar case, the arms simplify to three joint angles, one of which is the passive contact to the ground. As stated previously, the ground contact angle is dependent

on the shoulder and elbow joints. Hence, the ground contact angles are determined using (42). In the one-arm case, $n^2$ acceleration vectors must be computed where 'n' is the discretization of each of the independent joint angles.

$$\theta_1 = \frac{5\pi}{2} - \theta_3 - \theta_2. \qquad (42)$$

Similarly, for the two-arm model, the space now grows to $n^4$ samples, dramatically increasing the computational time. For the one arm case, n = 21, which results in 441 data points, while for the two-arm case, n = 12, which results in 20,736 data points. To counteract this drastic increase in space and visualization problems some assumptions were made to still allow an analysis of two arms. These assumptions include the mirrored and both arms equal. The mirrored assumption represent results when the left arms looks identical to the right arm hence by knowing the right arm configuration the left arm configuration can also be computed. The arms equal configuration represents when both the angles in the left and right are offset by 180 degrees leading to two arms the look as if they are following each other as seen in Figure 37.

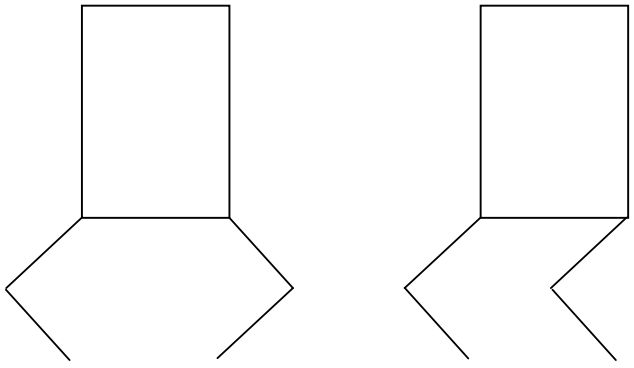

**Figure 37:** Left robot showing two arms mirror assumption and right robot showing both arms equal assumption

Figure 38 shows all the possible acceleration vectors over the entire sampled configuration space for the one-arm robot. These are the acceleration vectors as seen at the operational point which is chosen at the center rear of the robot body. The operational point was chosen at this point because it is a convenient place, on the physical robot, to apply the impulsive forces.

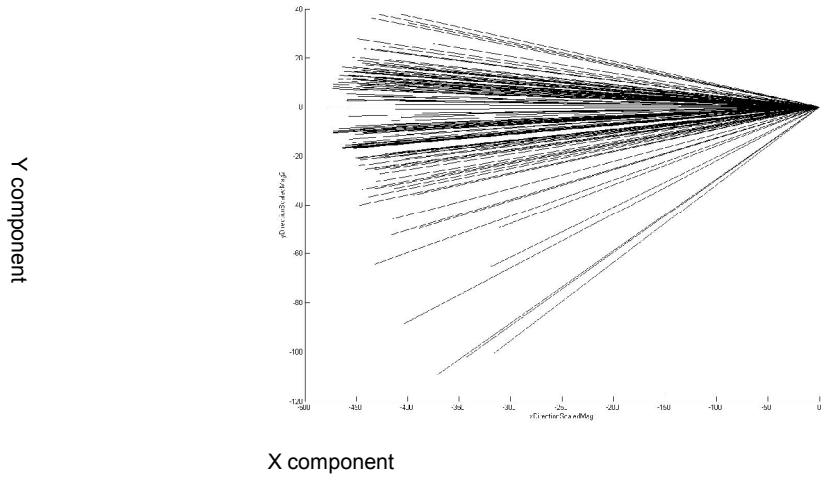


**Figure 38:** Possible acceleration vectors for the one-arm, planar case

The reason for the large scale in Figure 38 is due to the dimensions used in the model. These dimensions where based on the physical model built to test the Matlab model and are presented in Table 5 below.

**Table 5**: Model Specifications

| | **Left Arm Lower** | **Left Arm Upper** | **Right Arm Lower** | **Right Arm Upper** | **Body** |
|---|---|---|---|---|---|
| **Length (m)** | .06096 | .061976 | .06094 | .061976 | .06223 |
| **Width (m)** | .01397 | .01397 | .01397 | .01397 | .063246 |
| **Height (m)** | .024638 | .024638 | .024638 | .024638 | .038354 |
| **Mass (kg)** | .02472 | .02605 | .02454 | .02681 | .21034 |

The dimensions in Table 5 are relatively small compared to the unit magnitude impulse force used in the model and that is what causes the large magnitudes. In fact, the magnitude is of little importance as it is scaled by the magnitude of the impulse force. The direction of the accelerations is what allows us to steer the robot. With this mapping, Figure 38 shows us all the possible steering directions that can be selected to control the robot. With Figure 39, we can visualize highly sensitive and insensitive regions of the configuration space and interpolate between acceleration vectors to fine tune control.

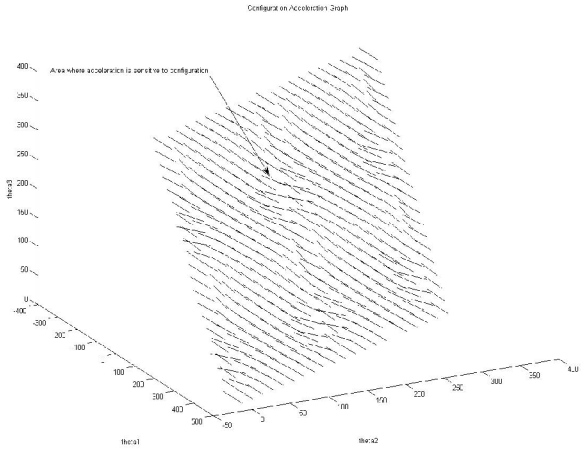


**Figure 39:** Configuration Space acceleration Plot

Figure 39 above is for the one-arm model which can be intuitively broken into a 3-D configuration space plot where 'x', 'y', 'z' represent $\theta_1$, $\theta_2$ and $\theta_3$, respectively. ($\theta_1$ is a dependent variable). Figure 38 clearly shows how acceleration is a function of configuration and how some places in the configuration space are more sensitive to a sudden angle change than others. Figure 38 and Figure 39 are intended to be used in tandem to assist in the planning of configuration-based acceleration trajectories.

### 6.3.2 Two Arms Simulation Results

When generating a discritized map, such as the one seen in Figure 38, for a two-arm configuration the space grows from a 3 dimensional one to a 6 dimensional one. To solve this problem, the two arm equal and the two arm mirror configuration is created allowing for a 3 dimensional method of representation. Figure 40 below shows the three dimensional space overlaying the one-arm model with the two-arm equal and mirror models. This figure is somewhat hard to understand as it is very dense. The different arrow colors show the different model assumptions. For this reason Figure 41 shows a selection of interesting points in the discritzed space showing how having two arms does allow for different acceleration as apposed to just one arm.

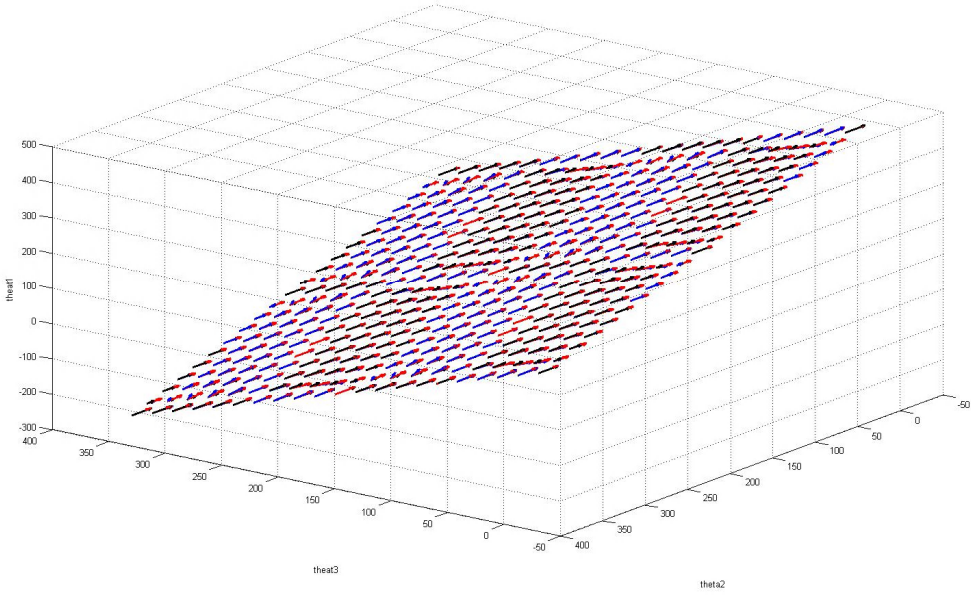


**Figure 40:** A three dimensional representation of both one arm disrctized space and the two-arm equal and two arm mirror space.

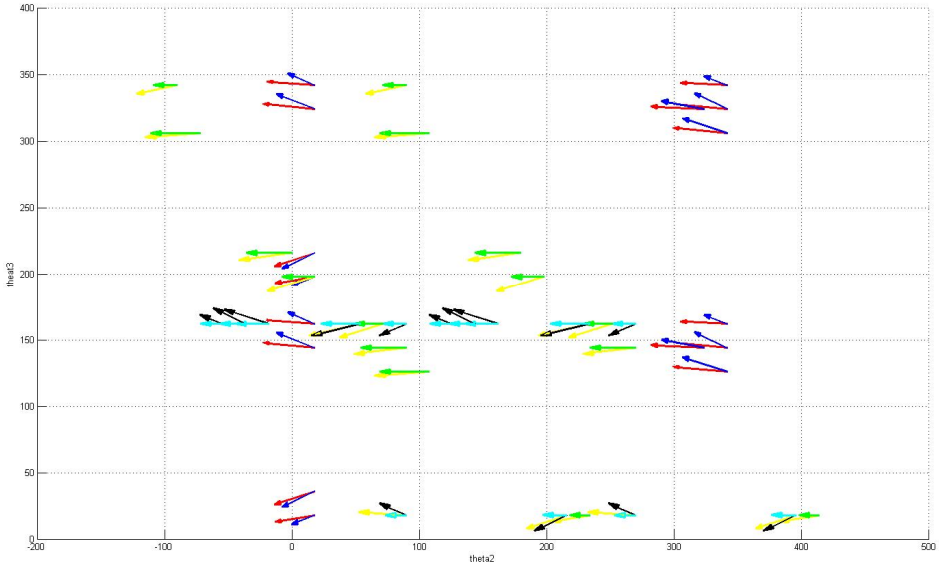


**Figure 41:** Points of interest between one arm and two-arm configuration causing different accelerations

### 6.3.3 One Arm, One Body, Experimental Results

In order to validate our planar Matlab models, a physical model was built, shown in Figure 42. The model consists of a robot body, removable two-link arms and a pin at the end of each arm for simulating a passive ground contact joint. A pendulum consisting of a hammer and a pin joint was used to apply impulsive forces along the negative x axis of the robot body to correspond to the simulations.

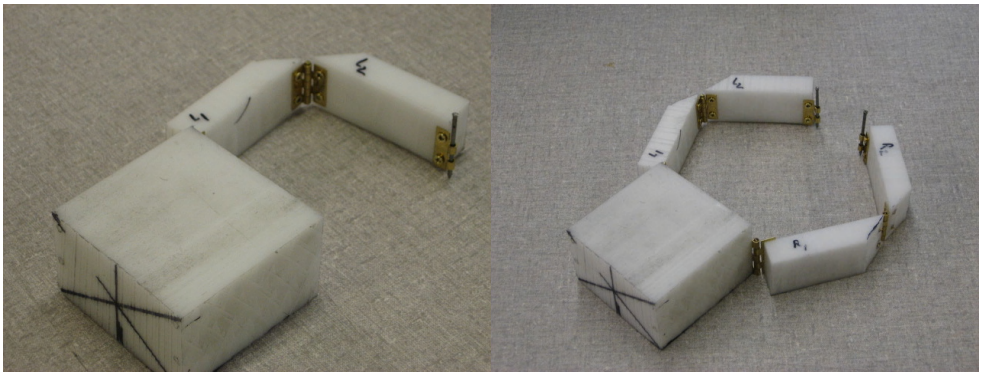

**Figure 42:** 1 arm model with pin for ground contact and 2 arm model with 'X' being the Operational Point

**Figure 43:** Pendulum setup

As previously mentioned, the operational point for the dynamic models was chosen at the point of impact in the back center of the robot body. The experiments were performed by placing the robot in a predefined configuration and the half hinges at the end of each arm were attached to a surface with a pin to keep them fixed in position but free to rotate. Then the hammer pendulum was pulled back to a pre-defined angle to impart a constant impulse for each trial. (The magnitude of the impulse was carefully chosen to provide good signal-to-noise, but to avoid so as to not cause the joints to reach physical limitations. Once the system came to rest, a line at the back of the robot was drawn to represent this new position and angle change of that line with respect to the original rest position line was recorded. Then the system was reset back to the initial configuration and four more trials were performed. Using a protractor, the angle of the body rotation was measured and compared to the Matlab results. Two joint configuration

sets where tested and the results are shown in Table 6. The two configuration sets chosen represent the extremes of body rotation to the left 'positive angle' and to the right 'negative angle'.

**Table 6:** Results from one-arm experiment

| Set 1 | | Set 2 | |
|---|---|---|---|
| **Run** | **Rotation Angle (deg)** | **Run** | **Rotation Angle (deg)** |
| 1 | 9 | 1 | -6 |
| 2 | 8 | 2 | -6 |
| 3 | 9 | 3 | -5 |
| 4 | 9 | 4 | 0 |
| 5 | 9 | 5 | -4 |

## 6.4 Analysis

### 6.4.1 One Arm

As seen in Figure 38, many different accelerations are possible, all in the negative 'x' direction. This is intuitively correct as the impulsive forces were applied in the negative 'x' direction and we do not expect to produce a negative mass. Again, when looking at results in Table 6 the general trend of the body rotation in either the positive or negative directions matches those results from the simulations. However, the exact magnitude of rotations between experiment and simulation does not match. The author believes that the reason for this discrepancy can be attributed to friction. The friction between the robot body and the surface along with the friction in the joints violate the first assumption used in the model. Additionally, the friction varied widely from trial to trial, manifesting itself in a large variance in the magnitudes of the motion of the body. (The distance of motion was not recorded as part of this experiment.) To get more detailed data on these high sensitivity areas, the joint space would need to be broken up

into more discrete steps or, at least, the regions of interest need to be further broken down.

### 6.4.2 Two Arms

It is interesting to note that all of the data was symmetric for both left and right arms. The range of angular rotation was +/- 13 degrees. Additionally, similar singularities were absorbed as those mentioned in the one arm configuration. Whenever the Robot was in a symmetric configuration, meaning the right arm was a mirror image of the left, the robot had a net forward acceleration that dominated the left-right acceleration. The reason a left or right acceleration was observed is because the two arms were not exactly identical in dimensions and mass as noted in Table 5. Additionally the point where the hammer hit the robot was not exactly in the center of the back as the OP in the model was.

## 6.5 Conclusion

This chapter showed a way of commanding a heterogeneous drive robot such as the TerminatorBot augmented with the water hammer by specifying angular and linear accelerations. These angular and linear translations need to be translated into an appropriate whole body mass matrix, which is created by controlling individual joints of the robot. Additionally this chapter demonstrated that use of the Operational Space with the augmented object for the derivation of effective mass matrix of a parallel link manipulator such as a gripper. As can be seen in both the one-arm and two-arm configuration the rotation of the body under the totally passive joints assumption 1 is +/- 13 degrees for two arms and -5 to +18 degrees in one arm, which both are fairly narrow. To increase the range, future work will look into implementing compliance control of the

joints as presented in [38]. The TerminatorBot for example has torque sensor in the elbow or joint 2/4 of the model, which can allow for controlling the torque at those points and theoretically increasing the range of motion.

# Chapter 7
# Conclusion and Future Work

## 7.1 Conclusion

This thesis presented both theoretical and practical approach for augmenting and controlling bulk motive drive regimes. These regimes include heterogeneous differential drive robots which were implemented in the form of the Crabinator augmented with the TerminatorBot. This robot was capable of improving the TerminatorBot side-slipping locomotion and showed how heterogeneous differential drive robot can be controlled where one half are arms masters and the other half is wheels slave. Additionally this research showed how to control another theoretical class of robots called heterogonous drive which is a more general form of heterogonous differential drive robots and are controlled via acceleration inputs not velocity inputs. This type of robot needs to be controlled through control of a mass matrix. And for parallel link actuators such as the ones on the TerminatorBot it was shown that can be d

one through the operational space regime with the augmented object.

## 7.2 Future Work

There are several ways the work done in this thesis can be expanded. Additional work can be done on differential drive robots showing that is possible to impalement this idea

on other robots other then the TerminatorBot augmented with the Crabinator Modules. Additionally there is great room for developing additional bulk motive force actuators for the resource constrained robots. Such work is already being done in the form of the water hammer actuators. The work done in modeling heterogonous drive needs to be expanded to six space moving away from the planer case. Since the TerminatorBot is designed as fingers more work as stated previously can be done on looking at the compliance of the system to see its sensitivity to different direction of force input.

## Bibliography

[1] J.J. Biesiadecki, E.T. Baumgartner, R.G. Bonitz, B.K. Cooper, F.R. Hartman, P.C. Leger, M.W. Maimone, S.A. Maxwell, A. Trebi-Ollenu, E.W. Tunstel, and J.R. Wright, "Mars exploration rover surface operations: Driving opportunity at meridiani planum," in Proc. IEEE Conf. Syst., Man, Cybern., The Big Island, HI, Oct. 2005, pp. 1823–1830.

[2] G. Seetharaman, A. Lakhotia, and E. P. Blasch. Unmanned Vehicles Come of Age: The DARPA Grand Challenge. Computer, 39(12):26–29, 2006.

[3] Yamachi, B, "PackBot: A Versatile Platform for Military Robotics," in Proceedings of SPIE: Unmanned Ground Vehicle Technology, v. 5422, April, 2004.

[4] Jennifer Carlson and Robin R. Murphy, "How UGVs Physically Fail in the Field", IEEE Transactions on Robotics, Vol. 21, No. 3, June 2005.

[5] M. Micire, "Analysis of the robotic-assisted search and rescue response to the world trade center disaster," master's thesis, Univ. South Florida, Tampa, Jul. 2002.

[6] D. Hougan, S. Benjaafar, J. Bonney, J. Budenske, M. Dvorak, M. Gini, H. French, D. Krantz, P. Li, F. Malver, B. Nelson, N. Papanikolopoulos, P. R. ans S.A. Stoeter, R. Voyles, and K. Yesin, "A miniature robotic system for reconnaissance and surveillance," in Proc. of the IEEE Int'l Conference on Robotics and Automation, 2000, pp. 501–507.

[7] A. Davids, "Urban search and rescue robots: from tragedy to technology," Intelligent Systems, IEEE [see also IEEE Intelligent Systems and Their Applications], vol. 17, no. 2, pp. 81–83, 2002, tY – JOUR.

[8] Borenstein, J., Hansen, J., and Nguyen, H., "The OmniTread OT-4 Serpentine Robot for Emergencies and Hazardous Environments," International Joint Topical Meeting: Sharing Solutions for Emergencies and Hazardous Environments, February 12-15, 2006, Salt Lake City, Utah, USA.

[9] Granosik, G., Hansen, M., and Borenstein, J., 2005, “The OmniTread Serpentine Robot for Industrial Inspection and Surveillance.” International Journal on Industrial Robots, Special Issue on Mobile Robots, Vol. IR32-2, March 18th, pp. 139-148.

[10] M. N Raibert, Legged Robots That Balance. Cambridge, MA: MIT Press, 1986.

[11] M. Hirose, Y. Haikawa, T. Takenaka, and K, Hirai, “Development of Humanoid Robot ASIMO,” Proc. Int. Conference on Intelligent Robots and Systems, Workshop2 (Oct.29, 2001), 2001.

[12] M. Raibert, K. Blankespoor, G. Nelson, R. Playter, “BigDog, the Rough-Terrain Quadroped Robot,” Proc. International Federation of Automatic Contro, Seoul Korea, July 6-11, 2008.

[13] John Rebula, Peter Neuhaus, Brian Bonnlander, Matthew Johnson, and Jerry Pratt. A controller for the littledog quadruped walking on rough terrain. In Proc. of the IEEE Int. Conf. on Robotics and Automation (ICRA), 2007.

[14] Masayuki, A., Takayama, T., and Hirose, S., “Development of " Souryu-III " Connected Crawler Vehicle for Inspection Inside Narrow and Winding Spaces. In IEEE/RSJ International Conference on Intelligent Robots and Systems, 2004.

[15] Guarnieri, M., P. Debenest, I. T. E. F. F. S. H., “Helios 7”, Journal of Robotics and Mechatronics, v. 141, pp. 171-177, 2003.

[16] Sheh, R., “The Redback: A Low-Cost Advanced Mobility Robot for Education and Research,” Proceedings of the 2006 IEEE International Workshop on Safety, Security and Rescue Robotics.

[17] Yamachi, B, "PackBot: A Versatile Platform for MilitaryRobotics," in Proceedings of SPIE: Unmanned Ground Vehicle Technology, v. 5422, April, 2004.

[18] M James C.M., David J.A., el al., “Torroidal Skin Drive for Snake Robot Locomotion”, in Proc. of IEEE International Conference on Robotics and Automation, Pasadena, CA, May 2008.

[19] Voyles, R.M. and A.C. Larson, “TerminatorBot: A Novel Robot with Dual-Use Mechanism for Locomotion and Manipulation", in IEEE/ASME Transactions on Mechatronics, v. 10, n. 1, pp. 17-25, 2005.

[20] Voyles, R.M., "TerminatorBot: A Robot with Dual-Use Arms for Manipulation and Locomotion," in Proceedings of the IEEE International Conference on Robotics and Automation, v 1, pp. 61-66, 2000.

[21] H. G. Nguyen, J. Morrell, K. Mullens, A. Burmeister, S. Miles, N. Farrington, K. Thomas, and D. Gage, “Segway Robotic Mobility Platform,” SPIE Proc. 5609: Mobile Robots XVII, Philadelphia, PA, October 2004.

[22] D. Balkcom, M. Mason, Time optimal trajectories for bounded velocity differential drive robots, Proceedings of the IEEE International Conference on Robotics and Automation 3 (2000) 2499–2504.

[23] K. Kozlowsk, K. Pazderski, “Modeling and Control of 4-Wheel Ski-Steering Mobile Robot,” in International Journal of Applied Math and Computer Science, Vol 14, n. 4, pp 477-496, 2004

[24] G. Indiveri, A. Nuchter, K. Lingemann, “High Speed Differential Drive Mobile Robot Path Folllowing Control With Bounded Wheel Speed Commands,” in Proc of 2007 IEEE conference on Robotics and Automation

[25] S. M. LaValle, Planning Algorithms, 2005. [Online]. Available: http://msl.cs.uiuc.edu/planning/

[26] R.M. Voyles, R. Godzdanker, T.H. Kim, "Auxiliary Motive Power for TerminatorBot: An Actuator Toolbox," in IEEE Workshop on Safety, Security and Rescue Robots, Rome, Italy, Sept., 2007, T4.

[27] Perrin, D.P., Kwon A., Howe R.B., “A Novel Actuated Tether Design for Rescue Robots Using Hydraulic Transients”, in Proc. of the 2004 IEEE International Conference on Robotics and Automation, pp 3482-3487, 2004.

[28] R. Godzdanker and R.M. Voyles, " Steering Control of an Active Tether Through Mass Matrix Control," in IEEE Workshop on Safety, Security and Rescue Robots, Sendai, Japan, Oct., 2008

[29] O. Khatib, “A unified Framework of Motion and Force Control of Robot Manipulators: The Operational Space Formulation”, in IEEE Journal of Robotics and Automation, v. RA-3, n. 1, pp. 43-53, 1987.

[30] D. Balkcom, M. Mason, Time optimal trajectories for bounded velocity differential drive robots, Proceedings of the IEEE International Conference on Robotics and Automation 3 (2000) 2499–2504.

[31] B.H. Kim, C. D'Souza, R.M. Voyles, J. Hersch, S. Roumeliotis, "A Reconfigurable Computing Platform for Plume Tracking with Mobile Sensor Networks," in the Proceedings of the SPIE Defense and Security Symposium, Orlando, FL, April, 2006.

[32] G. Gim and P.E. Nikravesh, “An analytical model of pneumatic tires for vehicle dynamic simulations. Part 1: pure slips,” in Intl. Journal of Vehicle Design, v. 11, n. 6, pp. 589-618, 1990.

[33] J. Lacombe, “Tire Model for Simulations of Vehicle Motion on High and Low Friction Road Surfaces,” in Proc. of the 2000 Winter Simulation Conference, pp. 1025-1034, 2000.

[34] J.M. Gere and S.P. Timoshenko, “Mechanics of Materials,” PWS-KENT Publishing, 1997.

[35] K.-S.Chang R. Holmberg and O. Khatib, “The Augmented Object Model: Cooperative Manipulation and Parallel Mechanism dynamics”, in Proceeding of the IEEE Conf. On Robotics and Automation, pp. 470-475, 2000.

[36] Khatib, O., “Object Manipulation in a Multi-Effector Robot System”, Robotics Research 4, Proc. 4th Int. Symposium, R. Bolles and B. Roth, eds., Cambridge: MIT Press, 1988, pp. 137-144.

[37] Craig J.C., “Introduction to Robotics Mechanics and Control”, Third edition, Pearson Prentice Hall, Upper Saddle River NJ, 2005.

[38] Cutkosky M.R., Kao I., “Computing and Controlling the Compliance of a Robotic Hand”, in IEEE Transaction on Robotics and Automation, v. 5, pp 151-165, 1989.

[39] B. Shamah, M. D. Wagner, S. Moorehead, J. Teza, D. Wettergreen, and W. L. Whittaker, “Steering and Control of a Passively Articulated Robot”, *SPIE, Sensor Fusion and Decentralized Control in Robotic Systems IV*, Vol. 4571, October, 2001.

[40] R.M. Voyles and R. Godzdanker, " Side-Slipping Locomotion of a Miniature, Reconfigurable Limb/Tread Hybrid Robot," in *IEEE Workshop on Safety, Security and Rescue Robots*, Sendai, Japan, Oct., 2008.

[41] U. Saranli, M. Buehler, and D. E. Koditschek. RHex: A simple and highly mobile hexapod robot. *The International Journal of Robotics Research*, 20(7):616–631, July 2001.

[42] Arai, M., Takayama, T., and Hirose, S. (2004). Development of Souryu-iii connected crawler vehicle for inspection inside narrow and winding spaces. In IEEE/RSJ International Conference on Intelligent Robots and Systems, 2004

[43] R. Merz, F.B. Prinz, K. Ramaswami, M. Terk and L.E. Weiss, Shape Deposition Manufacturing. In: H.L. Marcus *et al.Proceedings* of the 1994 Solid Freeform Fabrication Symposium (1994), pp. 1–8.

[44] http://rescue.isr.ist.utl.pt/index.php

[45] http://www.technovelgy.com/ct/Science-Fiction-News.asp?NewsNum=90

[46] http://www.robotworld.org.tw/index.htm?pid=10&News_ID=1070

[47] www.inuktun.com/sar.htm

[48] http://www.defensereview.com/more-robotic-infantry-soldiers-headed-to-afghanistan-and-iraq/

[49] http://www-robot.mes.titech.ac.jp/robot/wheeled/helios7/helios7.html

[50] http://rsheh.web.cse.unsw.edu.au/homepage/projects.html